Developing Stochastic Model of Thrust and Flight Dynamics for Small UAVs

A THESIS
SUBMITTED TO THE FACULTY OF THE GRADUATE SCHOOL
OF THE UNIVERSITY OF MINNESOTA
BY

Chandra Tjhai

IN PARTIAL FULFILLMENT OF THE REQUIREMENTS
FOR THE DEGREE OF
Master of Science

Demoz Gebre-Egziabher

September, 2013

Acknowledgements

I would like to take this opportunity to express my greatest gratitude for these individuals who had given contributions to my research during my career as a graduate student at the University of Minnesota. I would like to express my deepest appreciation to my advisor, Dr. Demoz Gebre-Egziabher, for his encouragement, guidance, and support in my research and study. Also, I would like to thank Dr. Peter Seiler and Dr. Nikolaos Papanikolopoulos for being my committee members.

I would like to express my appreciation to the people in my research group, Adhika Lie, Hamid Mokhtarzadeh, and Curtis Albrecht, for their supports in my research. I would like to thank James Rosenthal who was helping me in wind tunnel experiment. Also, I would like to thank Arion Mangio for his input in my prediction algorithm.

Lastly, I would like to express my gratitude to my parents, elder brother and sisters for their encouragement, inspiration, and support during my academic career at the University of Minnesota.

Abstract

This thesis presents a stochastic thrust model and aerodynamic model for small propeller driven UAVs whose power plant is a small electric motor. First a model which relates thrust generated by a small propeller driven electric motor as a function of throttle setting and commanded engine RPM is developed. A perturbation of this model is then used to relate the uncertainty in throttle and engine RPM commanded to the error in the predicted thrust. Such a stochastic model is indispensable in the design of state estimation and control systems for UAVs where the performance requirements of the systems are specified in stochastic terms. It is shown that thrust prediction models for small UAVs are not a simple, explicit functions relating throttle input and RPM command to thrust generated. Rather they are non-linear, iterative procedures which depend on a geometric description of the propeller and mathematical model of the motor. A detailed derivation of the iterative procedure is presented and the impact of errors which arise from inaccurate propeller and motor descriptions are discussed. Validation results from a series of wind tunnel tests are presented. The results show a favorable statistical agreement between the thrust uncertainty predicted by the model and the errors measured in the wind tunnel. The uncertainty model of aircraft aerodynamic coefficients developed based on wind tunnel experiment will be discussed at the end of this thesis.

Contents

List of Figures

Chapter 1

Introduction

Unmanned Aerial Vehicles (UAVs) are aircraft that operate autonomously (i.e., with no human operator on board) and are envisioned for use in many novel applications. These applications include but are not limited to surveillance, environmental monitoring, autonomous data gathering, traffic management and remote infrastructure inspection [1] [2]. UAVs come in a large range of sizes where the largest weigh several thousands of pounds and have wing spans on the order of hundreds of feet (e.g., Gobal Hawk). On the other end of the size spectrum are UAVs that weigh a few pounds, if not less, and have dimensions on the order of inches to tens of inches [3].

The use of small UAVs in operations that demand high reliability in and/or around populated areas will require that their performance be well understood and modeled [4] [5]. For example, the automatic pilots (or controllers) used to operate these vehicles must possess a high level of reliability and redundancy such that collisions with other vehicles, buildings or other infrastructure in avoided. This requires, in part, an accurate model of the UAV's dynamics be available to the designer of the automatic pilots [6]. While there are many off-the-shelf components and electronics for automatic control of small UAVs today, many of them are derivatives of similar components used on remote control airplanes flown for years by hobbyist. Many of these components are designed in an *ad-hoc* fashion and lack detailed mathematical models. Furthermore, their designs are neither supported by rigorous engineering analysis nor documentation which will allow to make precise predictions of their performance.

Thus, a method which allows constructing accurate mathematical models of aircraft

dynamics and thrust would be very useful in realizing the full potential of small UAVs. The work reported in this thesis is in line with the goal.

1.1 Summary of Previous Work

Developing dynamic model for aircraft is not new and methods exist that allow designers to construct such models easily. For example, DATCOM [7] provides a methodology for estimating aircraft aerodynamics, stability and control derivatives as a function of a aerodynamic and geometric description of an airplane. Similar methods are documented in well known design texts such as [8] and [9]. With respect to UAVs, these prior works have some limitations. First, many of the model in [7], [9] and [8] are empirically derived for aircraft that are much larger and fly much faster than many small UAVs. As such, it is difficult to match Reynolds numbers between the UAVs and those for which the methods in [7], [8] and [9] are valid. While it is possible to extrapolate (via interpolation) these empirical methods to the Reynolds number regimes of UAVs, it is not clear if such extrapolateions will yield accurate or meaningful results. Secondly, the models [7], [8] and [9] are not stochastic in nature. Thus, they are difficult to use in reliability analysis of guidance, navigation, and control system analysis.

The same is true for thrust models and the aeronautics literature contains works describing the propeller theory and/or propeller performance. The earliest propeller theory was developed by Rankine and R. E. Froude, and is known as the momentum theory. Later, Drzewiecki developed blade-element theory[10] which was an improvement on momentum theory. A further refinement in thrust prediction was afforded by the so called the vortex theory of propeller [11]. In the 1940s, for example, Theodorsen made a great improvement in propeller theory by studying lightly loaded and heavily loaded propeller using vortex theory [11]. References [12], [13], [14], and [15] are additional examples of related theoretical and experimental work from the same era aimed at predicting propeller performance. The limitation in computation resources in 1940 precluded the use of numerical models for thrust prediction. In view of computer resources available today, there has been a resurface of computational methods. Examples of recent work dealing with procedures of computing propeller performance include [16], [17] and [18].

The only method to get accurate dynamic model is performing a wind tunnel experiment. This limitation is, in part, the impetus for the National Aeronautics and Space Agency (NASA) at Langley Research Center program to develop a Free-flying Aircraft for Sub-scale Experimental Research (FASER) project. FASER's goal is to explore advanced methods for experiment design, data analysis, dynamic and control design [19].

However, the same limitations as aircraft dynamic models exist for thrust models. That is, it is not clear if the large body of experimental data and empirical models are accurate for small UAVs. Furthermore, existing models are not stochastic in nature and, thus, difficult to use in reliability analysis.

1.2 Thesis Contribution

There are three main objectives of this thesis. The first objective is to develop a computer tool which can be used to compute the propeller performance and verify the result with experimental result. This computation tool is based on the procedures presented by McCormick [16] which, in turn, is based on earlier work such as those in [10] - [18]. The second objective is to create a stochastic propeller performance curves by comparing the error from wind tunnel experiment and prediction made by the propeller performance model developed in this thesis. The third objective is to develop a method for constructing stochastic aircraft dynamic from wind tunnel and flight test data. The method will be validated using a small UAV, Mini Ultra-Stick.

1.3 Thesis Outline

In view of the above, this thesis is organized as follow: Chapter 2 presents a brief summary of propeller theory and the algorithm developed in this thesis to compute propeller performance. Chapter 3 presents the results of experiment used to validate the computational model developed in Chapter 2. Chapter 4 presents the theory and method for developing stochastic aircraft dynamic model. Chapter 5 presents a summary and concluding remarks as well as some suggestions for future work.

Chapter 2

Thrust Model

This chapter discusses the mathematical models for predicting the magnitude of thrust produced by a propeller. It discusses two well known models: the Momentum theory model and the blade-element theory model. It will be shown that an effective thrust model for a UAV will require elements of both theories. Thus, a combined thrust model is presented and a numerical code for implementing the combined thrust model is presented. The theory developed will be validated via experiment data in the next chapter.

2.1 Propeller Performance Metrics

Before discussing the details of thrust models, we will first present terminology and metrics used to describe propeller performance. Propellers can be thought of as heavily twisted wings. As wings produce lift when moving through the air so do propellers produced thrust ("a lifting" force in the direction of flight) when rotating. The propeller blades have a certain cross sections shaped like airfoil. These airfoils are similar airfoils used on conventional aircraft wings. The blade's cross section is sharp on the trailing edge and well-rounded on leading edge. The blade is oriented such that the sections near the hub have large blade angle and the sections near the tip have small blade angle. Blade angle is defined as the angle between the plane of rotation and the chord line of particular blade cross section. A typical propeller blade and the blade angle are shown in Fig. 2.1.

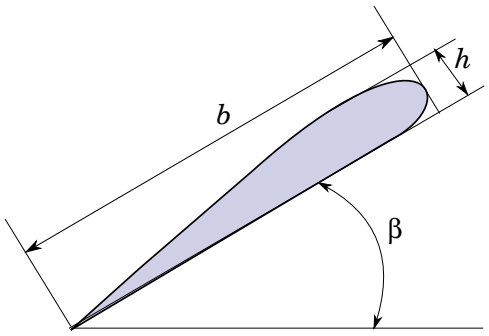

Figure 2.1: Blade-element's geometry

Propeller performance is described by the thrust produced, T, and the power, P, required to produce the corresponding thrust. Propeller thrust is defined to be the resultant force in the direction parallel to the propeller axis [20]. The propeller power is closely related to the torque put into the propeller which in turn, is a function of the power of the engine used to rotate the propeller. Propeller performance parameters are normally expressed, in terms of the non-dimensional quantities, thrust coefficient, C_T, and power coefficient, C_P, or torque coefficient, C_Q. The coefficients are related to thrust, T and torque, Q, by the following equations:

$$T = \rho n^2 D^4 C_T \tag{2.1}$$

$$Q = \rho n^2 D^5 C_Q \tag{2.2}$$

where n is propeller angular velocity, ρ is density of the air in which the propeller is operating and D is the propeller blade diameter. Torque and power are related by

$$P = 2\pi n Q$$

Thus, we can define another coefficient - the power coefficient - which is related to power by:

$$P = \rho n^3 D^5 C_P \tag{2.3}$$

In this non-dimensional form, C_Q and C_P are related by a constant, 2π, (i.e., $C_P = 2\pi C_Q$). Another non-dimensional quantity used in the analysis of propeller performance is the advance ratio, J, which is defined as:

$$J = \frac{V}{nD} \tag{2.4}$$

where V is the forward speed of the aircraft, n is propeller angular velocity and D is propeller diameter. The advance ratio is normally used as the independent parameter from which the dependent parameters C_T, C_Q, and C_P.

2.2 Momentum Theory

The momentum theory model attempts predict thrust by estimating the momentum change of the airflow that occurs as it passes through the propeller. To this end, the rotating propeller is idealized as an actuator disc; a device which produces thrust by accelerating the air in front of the disk so that it has a larger momentum as it leaves behind the disc. From Newton's second law it follows that a force (thrust) will be produced as a result of this momentum change. Momentum theory is one of the simplest theories to analyze propeller performance. Rankine and R. E. Froude developed this simple momentum theory [21] and its main parameter is the mass flow of air through the disc. Froude developed his theory based on the existence of the actuator disc meanwhile Rankine developed it by dividing this disc into many annular rings. Since this theory has only one parameter - the flow of the air - it can only represent an ideal performance of the propeller.

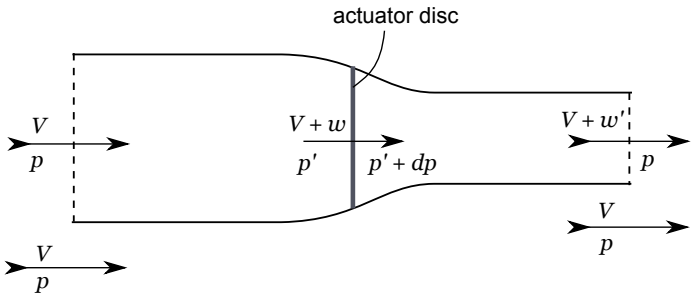

Figure 2.2: Flow around an actuator disc

Mass flow of air into a rotating propeller is shown in Fig. 2.2. The flow far in front of the disc has velocity of V and pressure of p. As the flow approaches the disc its velocity is increased by w immediately in front of the disc. The pressure in front of the disc becomes p' and increases further by dp behind the disc. The velocity far behind the disc will be different from V and the velocity immediately in front of the disk. We will

model this velocity magnitude change in front and far behind the propeller disc as $V+w$ and $V+w'$, respectively. The quantities w and w' are called the induced velocities in front and far behind the propeller, respectively. If known, they characterize the thrust production of a given propeller.

Applying Bernoulli's principle, the propeller performance equations can be derived. According to Bernoulli's principle, there must be a discontinuity at the actuator disc. The total pressure far in front of the disc and immediately in front of the disc are the same. The total pressure far behind the disc and immediately behind the disc are the same. Let us denoted C_1 and C_2 to be the total pressure in front of and behind the disc, respectively. Then using Bernoulli's principle, we can write:

$$C_1 = p + \frac{1}{2}\rho V^2 = p' + \frac{1}{2}\rho(V+w)^2 \tag{2.5}$$

$$C_2 = p' + dp + \frac{1}{2}\rho(V+w)^2 = p + \frac{1}{2}\rho(W+w')^2 \tag{2.6}$$

Then, the total pressure difference at the actuator disc is

$$\Delta p = C_2 - C_1 = p + \frac{1}{2}\rho(V+w')^2 - p - \frac{1}{2}\rho V^2 = \rho w'\left(V + \frac{w'}{2}\right) \tag{2.7}$$

Let A be the area of the actuator disc which is a function of propeller diameter or $A = \pi D^2/4$. For the moment, we will write this just as A. Then the thrust produced by the propeller is

$$T = \Delta p A = \rho A w'\left(V + \frac{w'}{2}\right) \tag{2.8}$$

To relate w' to w, another equation for thrust can be derived from the rate of change of axial momentum. That is,

$$T = \dot{m} \times \Delta\text{Velocity} = \rho A(V+w) \times [V + w' - V] = \rho A(V+w)w' \tag{2.9}$$

Using Eq.2.8 and Eq.2.9, the relation between w and w' can be determined by:

$$T = \rho A w'\left(V + \frac{w'}{2}\right) = \rho A(V+w)w'$$

and, thus,

$$w' = 2w \tag{2.10}$$

The induced velocity, w, can be determined using this momentum theory. To do this, we can rewrite Eq.2.9 by using Eq.2.10 as follows:

$$w^2 + Vw - \frac{T}{2\rho A} = 0$$

Solving the quadratic equation above for w,

$$w = -\frac{1}{2}\left[-V + \sqrt{V^2 + \frac{2T}{\rho A}}\right] \tag{2.11}$$

The second solution for the quadratic equation (i.e., $w < 0$) is ignored because it does not make physical sense. Since V is the freestream or forward velocity, then w will be maximum when the aircraft is not moving forward. Thus, we can solve for the induced velocity and it will be directly proportional to the thrust produced. That is,

$$w = \sqrt{\frac{T}{2\rho A}} \tag{2.12}$$

From basic thermodynamics we know that power added into the flow is the rate of change of work done on the fluid. Considering the flow immediately in front of the propeller, the power imparted to the flow (or induced in the flow) by the propeller is called the induced power, P_i, and is given by

$$P_i = \Delta p A(V + w)$$

Using Eq.2.7 and Eq.2.10 we can rewrite this as:

$$P_i = \rho w' \left(V + \frac{w'}{2}\right) A(V + w) = \rho A w'(V + w)^2 \tag{2.13}$$

The thrust produced by the propeller pushes the vehicle it is attached to forward at a velocity V. Thus, the net power output of the propeller (denote P_o) is equal to:

$$P_o = TV = \rho A w'(V + w)V$$

Note that P_o is not necessarily equal to P_i. That is, some of the energy that is imparted to the flowing air is lost and does not end up producing thrust. For example, some of it goes to imparting rotational motion to the air which is not useful in producing thrust.

The propeller efficiency, η, is a measure of how much of the induced power is lost. Using Eq.2.9, the efficiency of the propeller can be written as:

$$\eta_i = \frac{P_o}{P_i} = \frac{\rho A w'(V+w)V}{\rho A w'(V+w)^2} = \frac{1}{1+\frac{w}{V}} \tag{2.14}$$

This efficiency is called the ideal efficiency of the propeller. In actual application, the propeller performance will never reach this ideal efficiency value. The reasons are the ideal performance ignores the losses due to torque from propeller profile drag; blade tip and hub losses; and effect of number of blades.

2.3 Simple Blade-Element Theory

Blade-element theory was developed by Drzewiecki [10] [21] [22] in the early part of the 20^{th} century to help design of aircraft propellers. This theory performs better in predicting thrust than the simple momentum theory. This is because, in part, it considers the aerodynamic properties of the propeller. That is, the blade-element theory takes into account the twisted blade and aerodynamic coefficients of the airfoils cross sections used to make up the propeller. Thus, the theory can include the effects from profile drag and rotational torque in the performance calculation.

Blade-element theory divides the propeller blade into many small sections with a width of dr. This is shown in Fig. 2.3. Each section rotates about the center of the propeller hub which is located at a distance of r from a particular blade-element. Each element is an airfoil section with a chord length of b and maximum thickness of h. The blade is twisted such that each section is oriented at an angle β is called the twist or blade angle as was shown in Fig. 2.1.

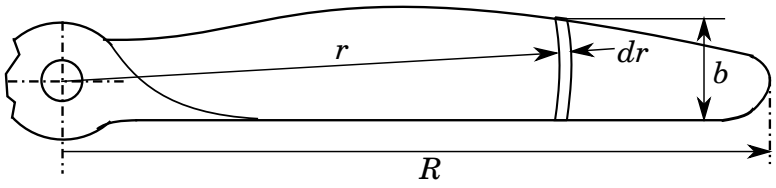

Figure 2.3: Blade-element at particular location from hub

Considering a propeller as an airscrew, the forward distance which the propeller screw itself forward in one revolution without slipping is called the pitch which is denoted

as $\hat{p}$. As shown in Fig. 2.4, the screw motion of blade element is the helical path AA' and its length $\hat{p}$ is given by [20]:

$$\hat{p} = 2\pi r \tan\beta$$

It is customary to normalize pitch by propeller diameter. This quantity is called pitch-diameter ratio and is given by:

$$\frac{\hat{p}}{D} = \pi x \tan\beta \tag{2.15}$$

where $x = 2r/D$ is the location of each blade-element as a fraction of propeller diameter. For a constant pitch propeller, the value of $\hat{p}$ is constant along the blade. This implies that the blade has a twist angle which varies along its length according to the following expression:

$$\beta = \tan^{-1}\left(\frac{\hat{p}/D}{\pi x}\right) \tag{2.16}$$

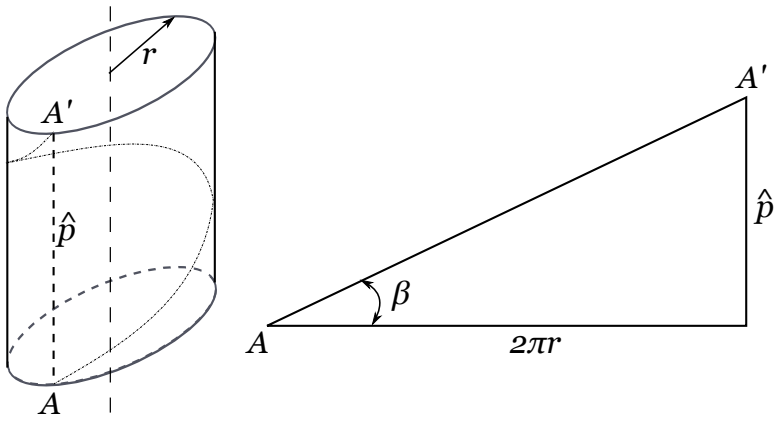

Figure 2.4: Helical path of blade-element's motion

A propeller blade performs two motion at the same time - a forward motion along with the aircraft, V, and rotation about the center of the hub, ωr. Due to these two motions, the blade section experiences a resultant velocity of magnitude V_R, oriented at an angle ϕ with respect to plane of rotation. Looking at each blade section as an airfoil with air flow passing through it, the airfoil will produce a differential aerodynamic force. However, if we are to consider the aerodynamics of each blade-element, we need to consider the effect of the induced velocity as well. The induced velocity, w, is the increase of the velocity of the air as it approaches the propeller. The vector addition

between V, ωr and w is shown in Fig. 2.5. The vector addition of these results in an effective velocity, V_E, which can be used in evaluating differential lift and drag of each blade element. Denoting them as differential lift dL and drag dD and using V_E we can write

$$dL = \frac{1}{2}\rho\, V_E^2\, b\, C_L\, dr \tag{2.17}$$

$$dD = \frac{1}{2}\rho\, V_E^2\, b\, C_D\, dr \tag{2.18}$$

Note that the induced angle of attack, α_i, is the result of induced velocity w and the effective velocity, V_E is the resultant velocity after adjustment of induced velocity. These differential forces will result in differential thrust and torque, dT and dQ, respectively.

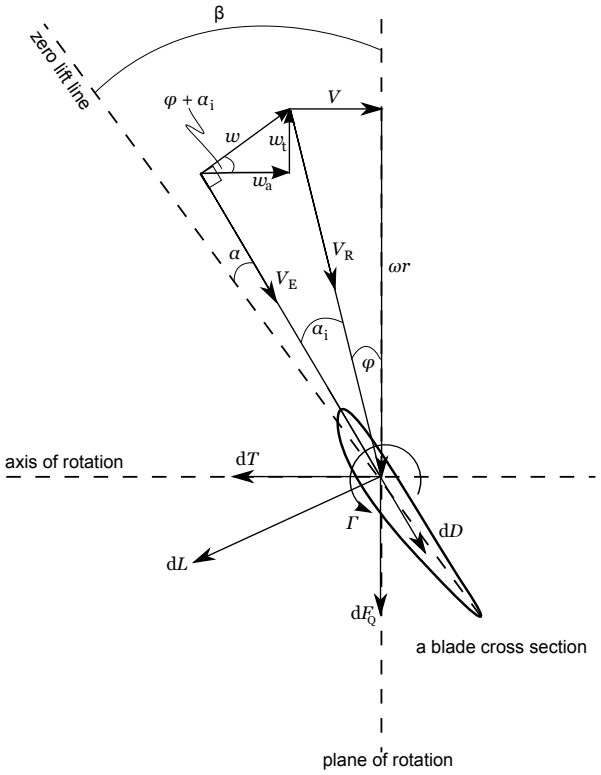

Figure 2.5: Velocities and forces acting on a blade element.

Using Fig. 2.5, the differential thrust and torque can be expressed as

$$dT = dL\ \cos(\phi + \alpha_i) - dD\ \sin(\phi + \alpha_i) \tag{2.19}$$

$$dQ = r[dL\ \sin(\phi + \alpha_i) + dD\ \cos(\phi + \alpha_i)] \tag{2.20}$$

From Eq.2.19 and Eq.2.20, we note that if we know the lift and drag polars for the airfoil cross section used to make the propeller as well as the induced velocity (for induced angle of attack), then we can numerically integrate these equations to predict thrust and torque. The challenge is to calculate w or α_i. We can address this challenge by combining blade element and momentum theories as we will do next.

2.4 Combined Momentum - Blade Element Theory

A modified theory which combines blade element theory with the momentum theory is called the combined momentum - blade element theory. The momentum theory contributes to the computation of the induced velocity which will give the information needed to compute induced angle of attack. From the momentum theory, we will rewrite Eq.2.8 as follow:

$$T = 2\rho A(V + w)w \tag{2.21}$$

A simplification to Eq.2.19 can be made by assuming that the induce angle of attack and drag-to-lift ratio are small such that $V_E \approx V_R$. Thus, Eq.2.19 can be used to approximate the differential thrust for B blades. Substituting Eq.2.17 into Eq.2.19,

$$dT = B\ \frac{1}{2}\ \rho\ V_R^2\ b\ C_L\ \cos\phi\ dr \tag{2.22}$$

Noting that $A = \pi r^2$, we can derive a differential thrust expression using Eq.2.21. This gives:

$$dT = d(2\rho(\pi r^2)(V + w)w) = 2\rho(2\pi r\ dr)(V + w)w \tag{2.23}$$

The induced velocity can be approximated as $w = V_R \alpha_i \cos\phi$. Using this in Eq.2.23 gives:

$$dT = 2\rho(2\pi r\ dr)(V + V_R\ \alpha_i\ \cos\phi)V_R\ \alpha_i\ \cos\phi \tag{2.24}$$

Equating Eq.2.22 with Eq.2.24, the expression for induced angle of attack can be derived. That is,

$$B\ \frac{1}{2}\ \rho\ V_R^2\ b\ C_L\ \cos\phi\ dr = \rho(2\pi r\ dr)(V + V_R\ \alpha_i\ \cos\phi)2V_R\ \alpha_i\ \cos\phi$$

Rearranging the expression above and substituting $C_L = C_{L\alpha}(\beta - \phi - \alpha_i)$,

$$B\ V_R\ b\ C_{L\alpha}(\beta - \phi - \alpha_i) = 8\pi r\alpha_i(V + V_R\ \alpha_i\ \cos\phi) \tag{2.25}$$

For simplicity of the mathematical expressions, we will non-dimensionalize Eq.2.25 by introducing the symbol σ called the solidity ratio and λ called local advance ratio. These quantities are expressed as follow:

$$\sigma = \frac{2B}{\pi}\ \frac{b}{D} \tag{2.26}$$

$$\lambda = \frac{V}{\frac{1}{2}\omega D} = \frac{V}{V_T} \tag{2.27}$$

Furthermore, since V_R is the resultant velocity of ωr and V, we will define the tip speed ratio as:

$$\frac{V_R}{V_T} = \sqrt{\lambda^2 + x^2}$$

Given these definitions, the flow angle ϕ is equal to

$$\phi = \tan^{-1}\left(\frac{\lambda}{x}\right) = \tan^{-1}\left(\frac{J}{\pi x}\right) \tag{2.28}$$

Using these non-dimensional parameters, Eq.2.25 can be simplified and expressed as a quadratic equation for induced angle of attack. That is,

$$\alpha_i^2 + \left[\frac{\lambda}{x} + \frac{\sigma C_{L\alpha} V_R}{8x^2 V_T}\right]\alpha_i - \frac{\sigma C_{L\alpha} V_R}{2x^2 V_T}(\beta - \phi) = 0$$

Solving this equation gives the following expression for α_i as a function of x:

$$\alpha_i = \frac{1}{2}\left[-\left(\frac{\lambda}{x} + \frac{\sigma C_{L\alpha}}{8x^2}\sqrt{\lambda^2 + x^2}\right) + \sqrt{\left(\frac{\lambda}{x} + \frac{\sigma C_{L\alpha}}{8x^2}\sqrt{\lambda^2 + x^2}\right)^2 + \frac{\sigma C_{L\alpha}}{2x^2}\sqrt{\lambda^2 + x^2}(\beta - \phi)}\right] \tag{2.29}$$

The negative solution for α_i is not used because it represents the case where the induced velocity is in the direction of flight: A physical impossibility in normal flight.

Using α_i, propeller performance parameters, thrust and power, can be computed by numerical integration of Eq.2.17 - Eq.2.20.

$$T = \int \frac{1}{2}\rho\ V_E^2\ B\ b\ [C_L\ \cos(\phi + \alpha_i) - C_D\ \sin(\phi + \alpha_i)]\ dr$$

$$P = \omega \int \frac{1}{2}\rho\ V_E^2\ B\ b\ r[C_L\ \sin(\phi + \alpha_i) + C_D\ \cos(\phi + \alpha_i)]\ dr$$

For computational purposes, it is preferred to have these parameters in non-dimensional form. Using the definition given at the beginning of this chapter, we can write:

$$C_T = \frac{\pi}{8}\int_{x_h}^{x_T}(J^2+\pi^2x^2)\sigma[C_L\cos(\phi+\alpha_i)-C_D\sin(\phi+\alpha_i)]dx \tag{2.30}$$

$$C_P = \frac{\pi}{8}\int_{x_h}^{x_T}\pi x(J^2+\pi^2x^2)\sigma[C_L\sin(\phi+\alpha_i)+C_D\cos(\phi+\alpha_i)]dx \tag{2.31}$$

Eq.2.30 and Eq.2.31 can be solved by numerical integration from the station near the hub, x_h, to the station near the tip, x_T.

2.5 Incorporating Vortex Theory

The blade element theory has a limitation resulting from at least two assumption. First, it assumes that blade elements at different station do not affect the flow of each other. Secondly, it assumes that w is normal to the propeller disc. The net effect of this is that the estimate of w is not correct. Vortex theory provides a means by which the estimate of w can be improved. The idea is akin to what is done in thin-airfoil theory [23] [24]. The blade is replaced by a bound vortex distribution and, thus, the interaction of the flow at different sections can be accounted for.

Theodorsen[11] presented the solution of the optimum distribution for heavily loaded propeller using the circulation distribution developed by Goldstein who had presented the distribution for lightly loaded propeller. Using Goldstein's vortex theory, the induced velocity can be related to the bound vortex circulation, Γ, by

$$w_t = \frac{B\Gamma}{4\pi r\kappa} \tag{2.32}$$

where κ is Goldstein's κ factor. This factor is normally given in tabulated form as function of radial position, local advance ratio and number of blades. For details on this, see references [11] and [17].

An approximation for Goldstein's κ factor is Prandtl's solution of tip loss factor. Prandtl's tip loss factor, F, gives good results for propellers that have a large number of blades and operating at small advance ratio.

$$F = \frac{2}{\pi}\cos^{-1}\exp\left[-\frac{B(1-x)}{2\sin\phi_T}\right] \tag{2.33}$$

where ϕ_T is the flow angle at the tip and it is given by:

$$\phi_T = \tan^{-1} \frac{V}{V_T}$$

This gives us a way to estimate the tangential component of w. However, from Fig. 2.5 we know that the induced velocity ,w, consists of axial and tangential components, w_a and w_t, respectively. They are related by

$$\tan(\alpha_i + \phi) = \frac{V + w_a}{\omega r - w_t} = \frac{w_t}{w_a}$$

We can solve the expression above to obtain an expression for w_a as function of w_t:

$$w_a = \frac{1}{2}\left[-V + \sqrt{V^2 + 4w_t(\omega r - w_t)}\right]$$

For computational purposes, w_a can be expressed in a non-dimensional form as:

$$\frac{w_a}{V_T} = \frac{1}{2}\left[-\lambda + \sqrt{\lambda^2 + 4\frac{w_t}{V_T}\left(x - \frac{w_t}{V_T}\right)}\ \right] \tag{2.34}$$

Once we calculate w_a/V_T, we can estimate w_t. To calculate w_t we start with Eq.2.32 where Goldstein's κ factor can be substituted by Prandtl's tip loss factor. The bound circulation can calculated using Kutta-Joukowski theorem.

$$\Gamma = \frac{1}{2} b C_L V_E \tag{2.35}$$

Thus, substituting Eq.2.35 into Eq.2.32 we can solve for w_t/V_T as:

$$\frac{w_t}{V_T} = \frac{BC_L}{4\pi x F}\ \frac{V_E}{V_T}\ \frac{b}{D} \tag{2.36}$$

The induced angle of attack, α_i can now be computed by the following expression,

$$\alpha_i = \tan^{-1}\left(\frac{V + w_a}{wr - w_t}\right) - \phi$$

In non-dimensional form, this expression is given as:

$$\alpha_i = \tan^{-1}\left(\frac{\lambda + \frac{w_a}{V_T}}{x - \frac{w_t}{V_T}}\right) - \phi \tag{2.37}$$

From Fig. 2.5, the remaining parameters can be derived. For example, using simple geometry we note that:

$$V_E^2 = (V + w_a)^2 + (\omega r - w_t)^2$$

For its non-dimensional form, substitute $V = \lambda V_T$ and $r = xR$,

$$\frac{V_E}{V_T} = \sqrt{\left(\lambda + \frac{w_a}{V_T}\right)^2 + \left(x - \frac{w_t}{V_T}\right)^2} \tag{2.38}$$

Reference [16], notes that this vortex theory needs two additional corrections for accuracy. These two corrections are:

1. The correction of angle of attack due to finite thickness of the blade element.

$$\Delta\alpha = \frac{4\lambda\sigma}{15(\lambda^2 + x^2)} \frac{h}{b} \tag{2.39}$$

2. The correction for C_L due to camber which results from the tangential component of induced velocity.

$$\Delta C_L = \frac{1}{4}\frac{\partial C_L}{\partial \alpha}\Delta\theta \tag{2.40}$$

where

$$\Delta\theta = \tan^{-1}\left(\frac{V + w_a}{\omega r - 2w_t}\right) - \tan -1\left(\frac{V + w_a}{\omega r}\right)$$

$$\Delta\theta = \tan^{-1}\left(\frac{\lambda + w_a/V_T}{x - 2w_t/V_T}\right) - \tan^{-1}\left(\frac{\lambda + w_a/V_T}{x}\right) \tag{2.41}$$

The local angle of attack, α, can be determined after the induced angle of attack is determined.

$$\alpha = \beta - \phi - \alpha_i - \Delta\alpha \tag{2.42}$$

When the lift and drag coefficients come from the known airfoil characteristics. The thrust and power coefficients can be derived using Eq.2.17 - Eq.2.20 as follow:

$$C_T = \frac{\pi^3}{8}\int_{x_h}^{x_T}\left(\frac{V_E}{V_T}\right)^2 \sigma[C_L\cos(\phi + \alpha_i) - C_D\sin(\phi + \alpha_i)]dx \tag{2.43}$$

$$C_P = \frac{\pi^4}{8}\int_{x_h}^{x_T}\left(\frac{V_E}{V_T}\right)^2 \sigma x[C_L\sin(\phi + \alpha_i) + C_D\cos(\phi + \alpha_i)]dx \tag{2.44}$$

2.6 Computational Estimation of Propeller Performance

The propeller performance computation algorithm developed in this thesis is based on the combination of blade element and vortex theory described in previous sections. The inputs are the following propeller geometry parameters: Propeller diameter, blade chord length, blade thickness, and blade pitch. The outputs are thrust coefficient, power coefficient and efficiency.

Implementation of this algorithm can be summarized as follow: First, the propeller blade is discretized into many small incremental segments. Second, at each blade element, the induced angle of attack is determined through an iterative method based on the vortex theory. Once the induced angle of attack is known, the local aerodynamic forces are determined using airfoil profile. Third, Eq.2.43 and Eq.2.44 or Eq.2.30 and Eq.2.31 are solved using numerical integration. Figure 2.6 presents an algorithmic flow chart of this propeller performance computation. Note that we use $f(\alpha)$ to represent the best mathematical function used that describes the lift polar of known airfoil cross section. In this paper, $f(\alpha)$ is a polynomial fit to a specific lift curve. The airfoil aerodynamic model used in the computation is linear lift curve and the drag is computed by:

$$C_D = C_{D0} + K\, C_L^2$$

The diagram of Fig. 2.6 shows an iteration step to get induced angle of attack, α_i. It should be noticed that there may be a case where this iteration does not converge. An example of this is the case where α_i becomes a complex number because w_a/V_T is a square-root of negative value. This is caused by the model of the lift curve used in the computation.

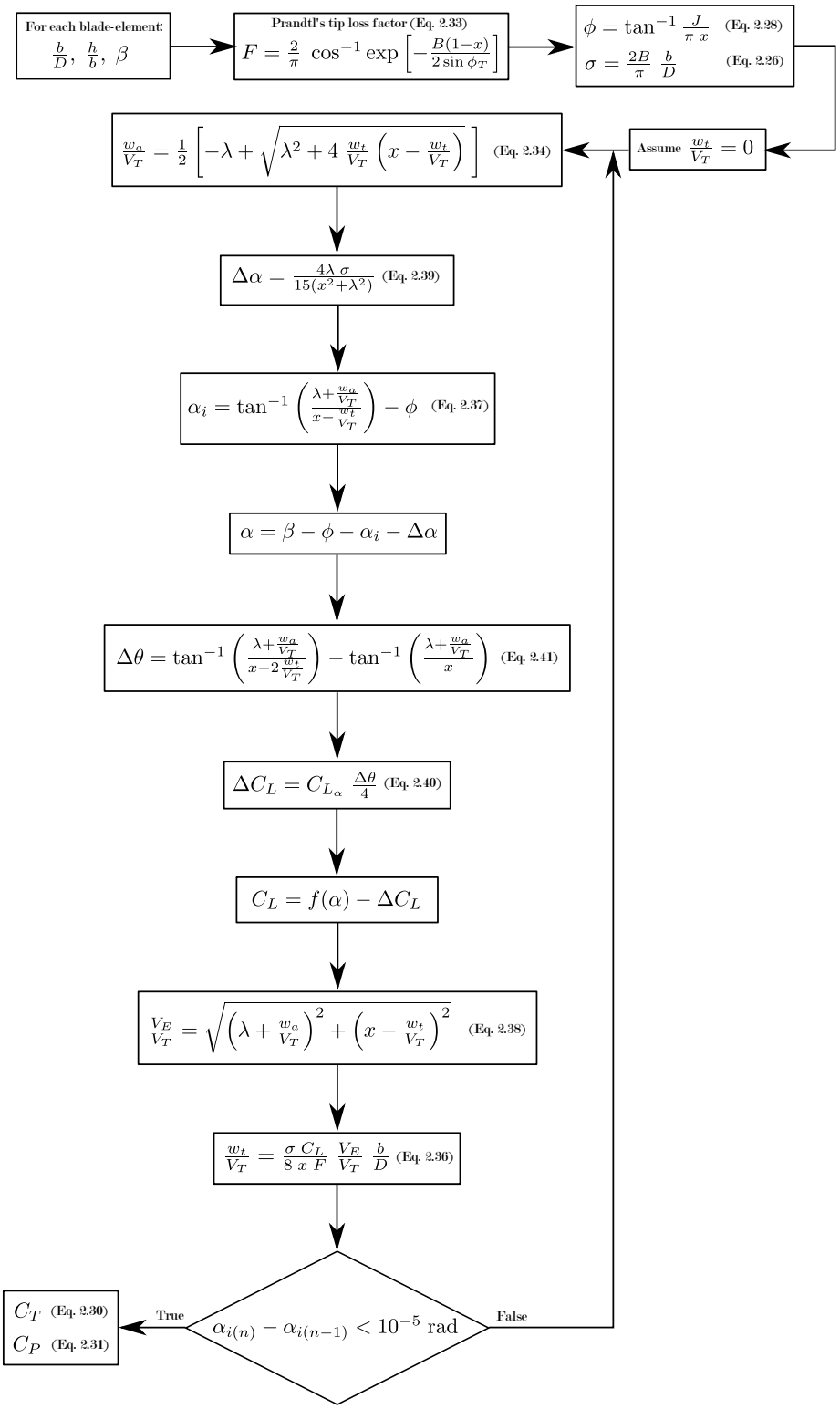

Figure 2.6: Flow chart of computation algorithm

Chapter 3

Experiment and Validation

In this chapter, the results of propeller performance computed using the method described in previous chapter are validated using experiment data. The experiments were performed using the wind tunnel facility as the University of Minnesota. This chapter describes the experiment procedures, implementation of the algorithm developed in previous chapter and discussion of both experimental and computational results.

3.1 Propeller Wind Tunnel Experiment

One of the methods to estimate propeller performance is to test the propeller in a wind tunnel. A large number of full-scale propeller tests had been done by the National Advisory Committee for Aeronautics (NACA) in 1930s and 1940s. This thesis explores a full-scale propeller test for UAVs. The size of the propellers are much smaller than the ones tested by NACA. Thus, part of the motivation for the work that follows is to examine how different in size of the propeller affects the applicability of the NACA historic test results on small propellers. In this section, we present procedures of thin electric propeller test.

3.1.1 Apparatus and Methods

The experiments were conducted using a closed-return wind tunnel at the University of Minnesota [25]. The wind tunnel is driven by 100 HP frequency controlled variable speed electric motor with P-38 Feathering Propeller. This wind tunnel has a 40×60

inches test section. The wind tunnel is equipped with a sensor which measures three axes of forces and three axes of torques.

The propeller tested in this experiment was made by Advanced Precision Composites (APC) Propellers and it is constant pitch propeller. This propeller has a pitch of 7 inches and 10 inches diameter. The main cross section shape is a NACA 4412 and/or Clark-Y airfoil section. The propeller geometry curve is shown in Fig. 3.1 [26].

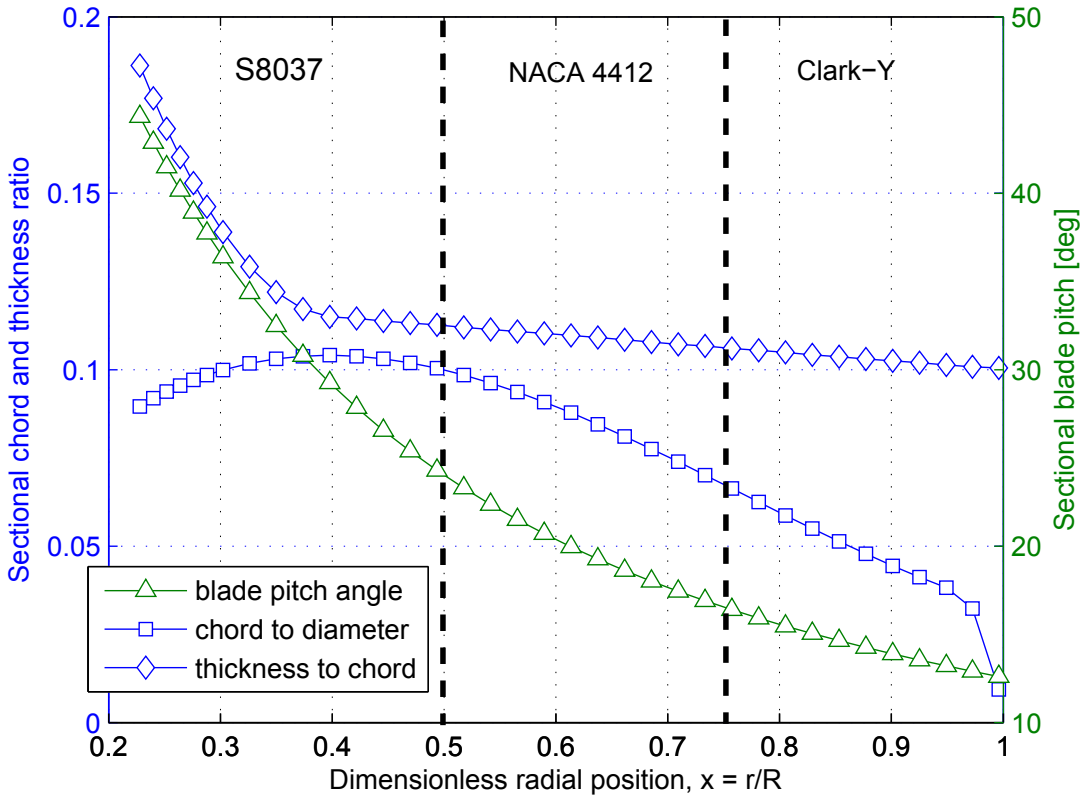

Figure 3.1: Geometric blade curves of 10 in. diameter and 7 in. pitch propeller (APC 10x7E).

The propeller is mounted to a brushless electric motor which is also mounted to the measurement sensor through a connector as shown in Fig. 3.2. The motor rotation

is measured by a RPM sensor mounted near the hub of the propeller. This sensor is connected to a simple circuit to measure a train of voltage pulses. The frequency of the voltage pulse is the rotational speed and is measured by an oscilloscope.

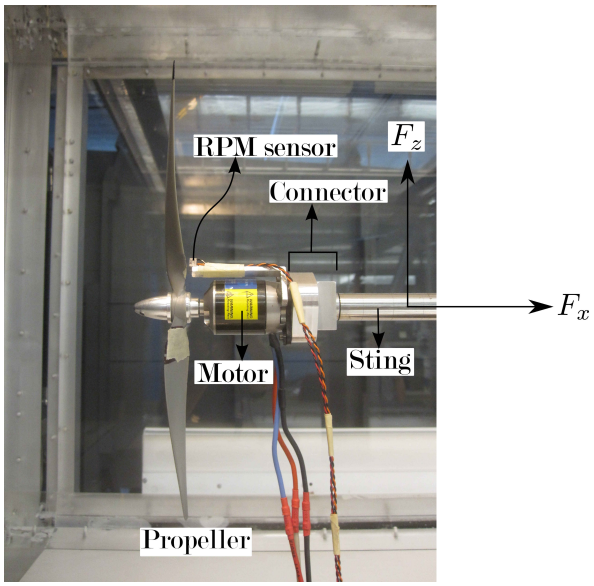

Figure 3.2: Propeller inside the test section.

The propeller was tested at different rotational speeds. The range of the motor rotation speeds for this experiment was between 4000 rpm to 6000 rpm. At each rotational speed, the wind speed is varied from 0 to a certain value for which the x-axis of force measurement showed a negative thrust. The negative thrust means that the propeller does not produce the forward force but it uses the wind energy to rotate.

3.1.2 Experimental Results

The data reduction of the propeller experiment is based on the equations from section 2.1. The coordinate system of the wind tunnel sensor is shown in Fig 3.2. F_X represents the axial force measurement and an axial torque Q_X is also measured by the sensor. Noticed that F_X is the net force sensed by the sensor and this force is not the total thrust produced by the propeller but it is corrupted by the aerodynamic drag of the

rotating system or fixture drag, F_d. Thus, the thrust produced by the propeller is:

$$T = -F_X + F_d$$

The fixture drag correction is based on the work done by Selig and Ananda [27].

$$F_d = \frac{1}{2}\,\rho\,(J\;n\;D)^2\;S_f\;C_{df}$$

where S_f is the motor fixture frontal area and C_{df} is assumed to be 1.

The experimental result of the propeller is shown in Fig. 3.3 and 3.4. These results show that the rotational speed affects the propeller performance due to Reynolds numbers. At lower rotational speed, the blade operates at lower Reynolds number and the Reynolds number increases as the rotational speed increases. Based on the airfoil aerodynamics, the propeller becomes more efficient as the Reynolds number increases.

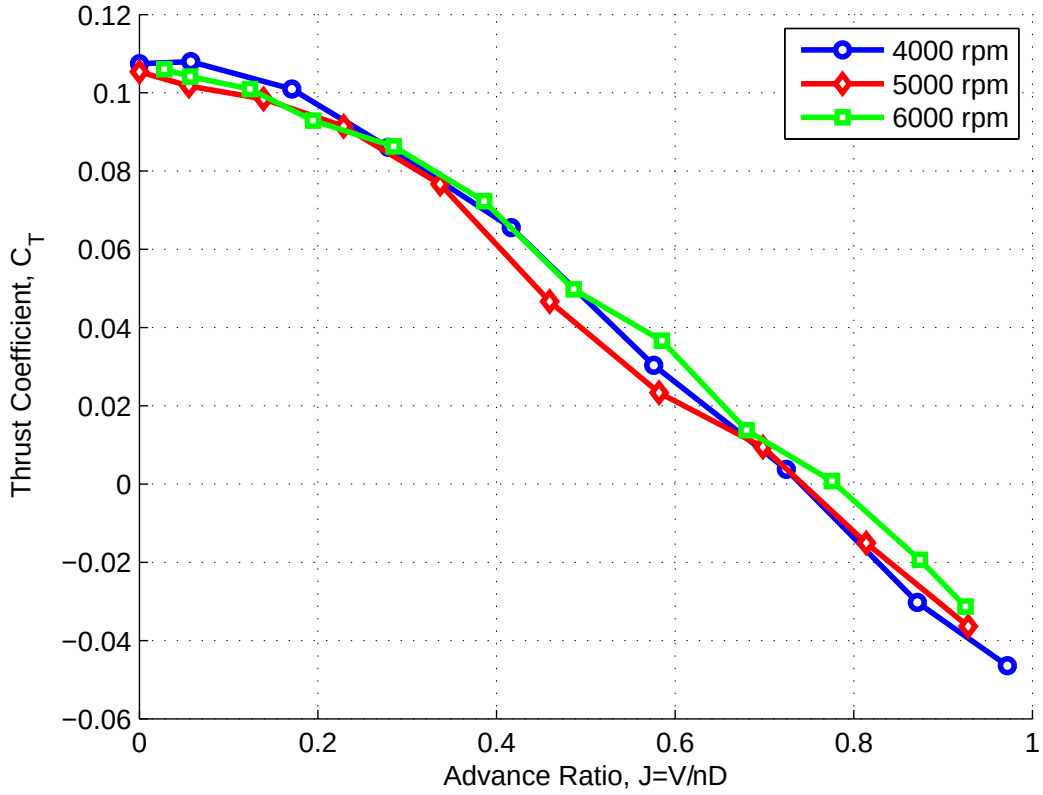

Figure 3.3: Thrust coefficient of APC 10x7E.

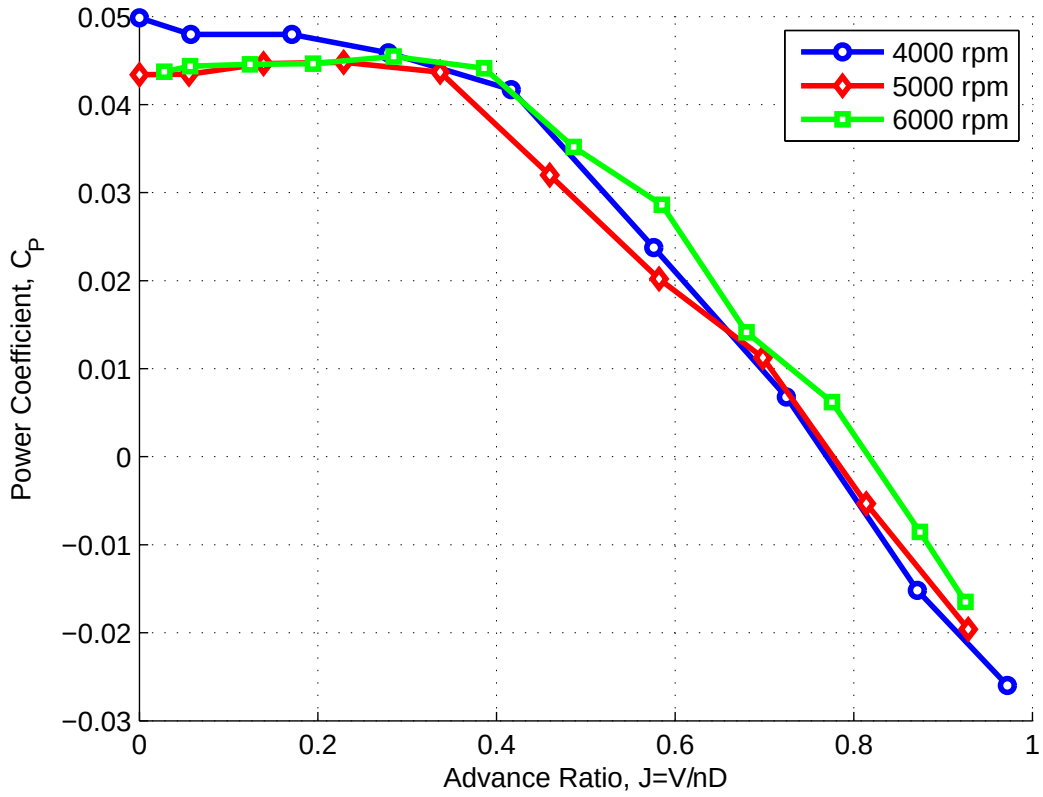

Figure 3.4: Power coefficient of APC 10x7E.

3.2 Propeller Performance Computation

We can now compare this data to the output of the algorithm developed in Chapter 2. This algorithm is implemented in MATLAB. The inputs are the propeller geometry and its cross section shapes. Based on blade element theory, the blade is divided into many small sections and each section has its own cross section shape. These cross section shapes are represented by some known airfoil shapes in the computation process. The airfoil shape is characterized by the thickness to chord ratio and the camber. Notice that most of the lift force is generated by the upper surface of the airfoil [10]. In most cases, a propeller blade can be represented by several airfoil cross sections. The computation

process is based on the description at the last section of Chapter 2.

3.2.1 APC 10x7E Propeller

This propeller's geometry is shown in Fig. 3.1. It has 10 in. diameter and a pitch of 7 in. per revolution. The actual propeller cross sections are non-standard airfoil shapes. These non-standard airfoils do not have the documantation of their aerodynamic characteristics. Thus, in the computation, the blade cross sections are represented by 3 known airfoil shapes. From hub to tip, they are S8037, NACA 4412, and Clark-Y. The S8037 covers 50% of the radial stations while NACA 4412 and Clark-Y cover 25% of the radial stations. Fig. 3.5 shows the blade cross sections with their representative airfoil shapes.

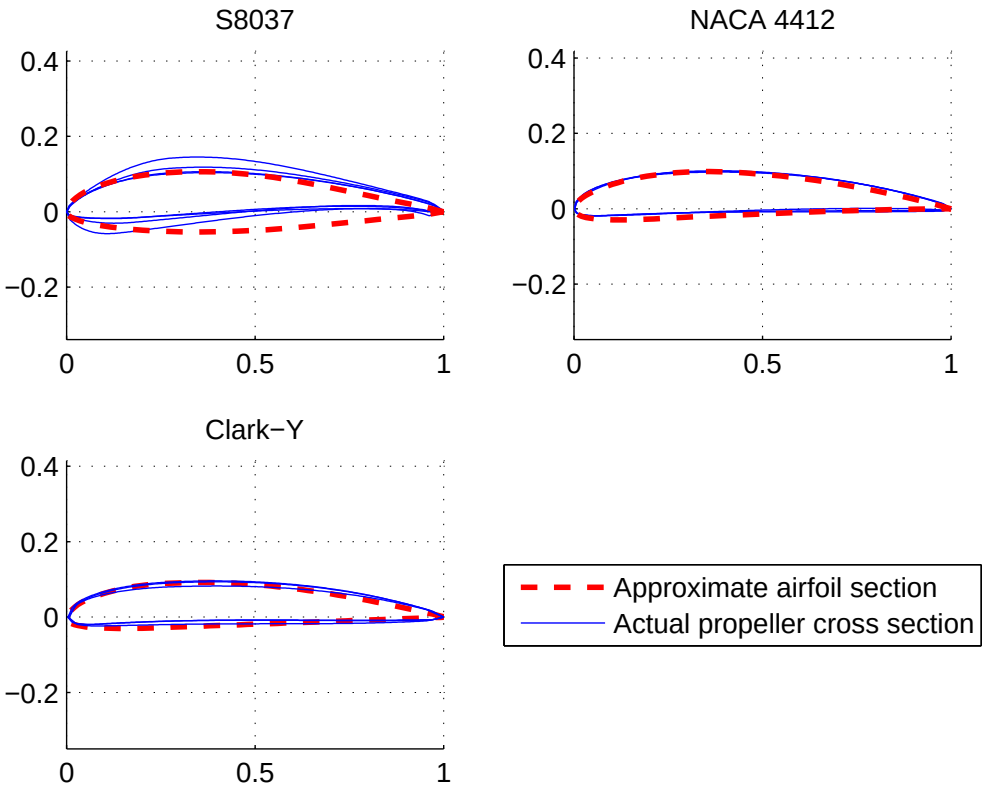

Figure 3.5: Blade cross sections of APC 10x7E.

The performance of APC 10×7E can be computed by importing its geometry (shown in Fig. 3.1) and selecting proper airfoil aerodynamics. The aerodynamics of the blade cross sections are represented by the known airfoils as shown in Fig. 3.5. However, there are some errors in the aerodynamic description. For example, the pitch angle assumed in the model may be different from the actual pitch angle. Another error considered in this regard is the slope of the lift curve for each blade element.

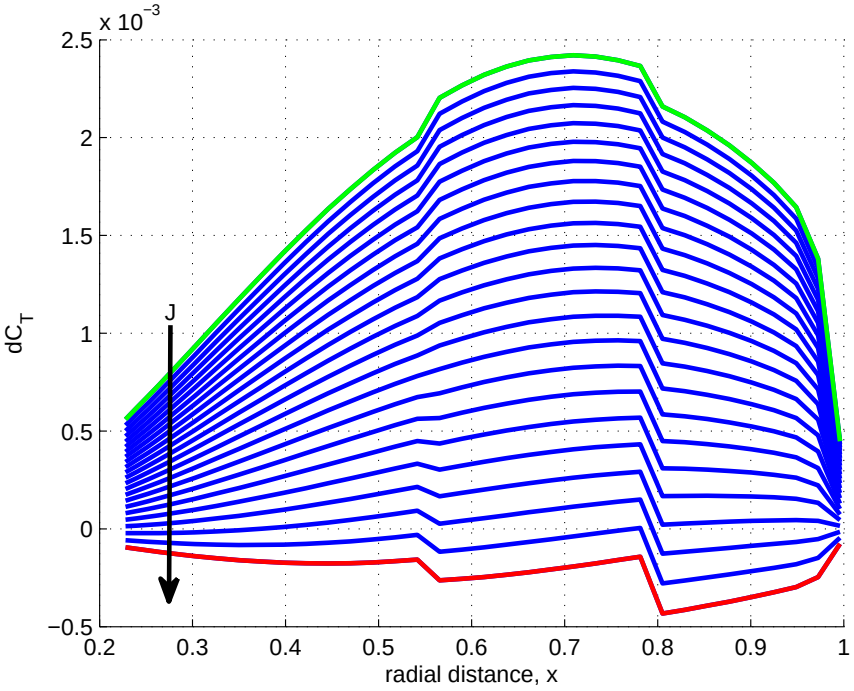

Figure 3.6: Sectional thrust coefficient of APC 10x7E.

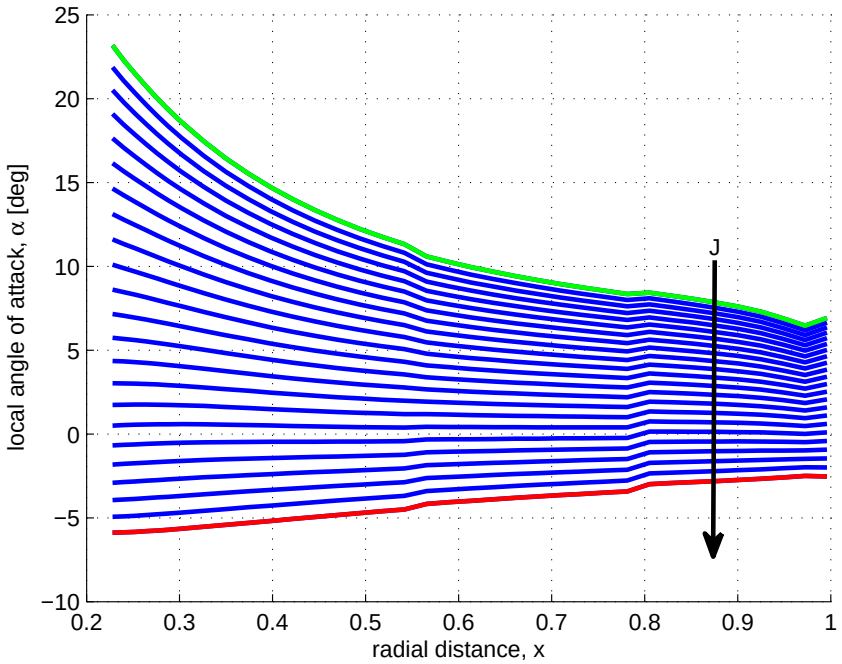

Figure 3.7: Sectional angle of attack of APC 10x7E.

As a baseline a simulation using a nominal model is performed and compared to experimental data. The computational result agrees with the experimental result as shown in Fig. 3.8 and Fig. 3.9. The sectional thrust coefficient from Fig. 3.6 shows that only a portion of the blade does most of the works. The sections near the root do not contribute a lot of thrust. This shows that the approximation of the aerodynamics of the sections near the root will not affect the result significantly. The local angle of attack decreases as the advance ratio increases as shown in Fig. 3.7. The blade operates at high angle of attack when the advance ratio is low and it operates at negative angle of attack when the advance ratio is high. The static thrust coefficient is 0.1138 and the static power coefficient is 0.0457. Both curves cross the zero line at advance ratio about 0.8.

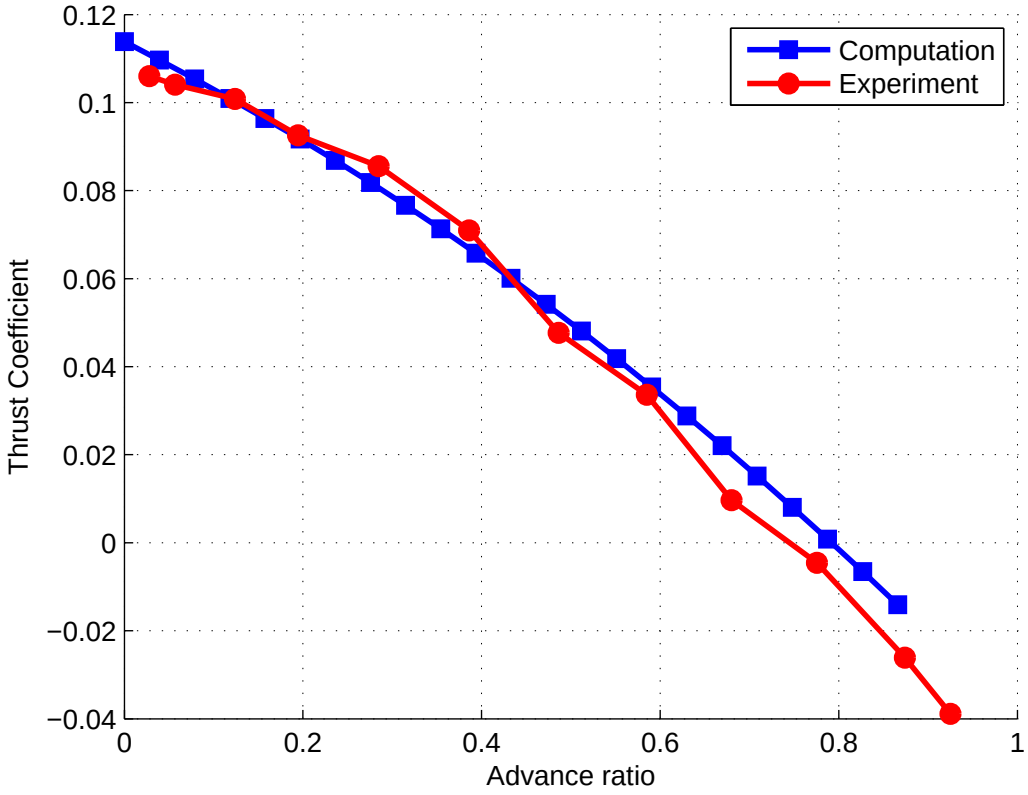

Figure 3.8: Propeller thrust estimation of APC 10x7E.

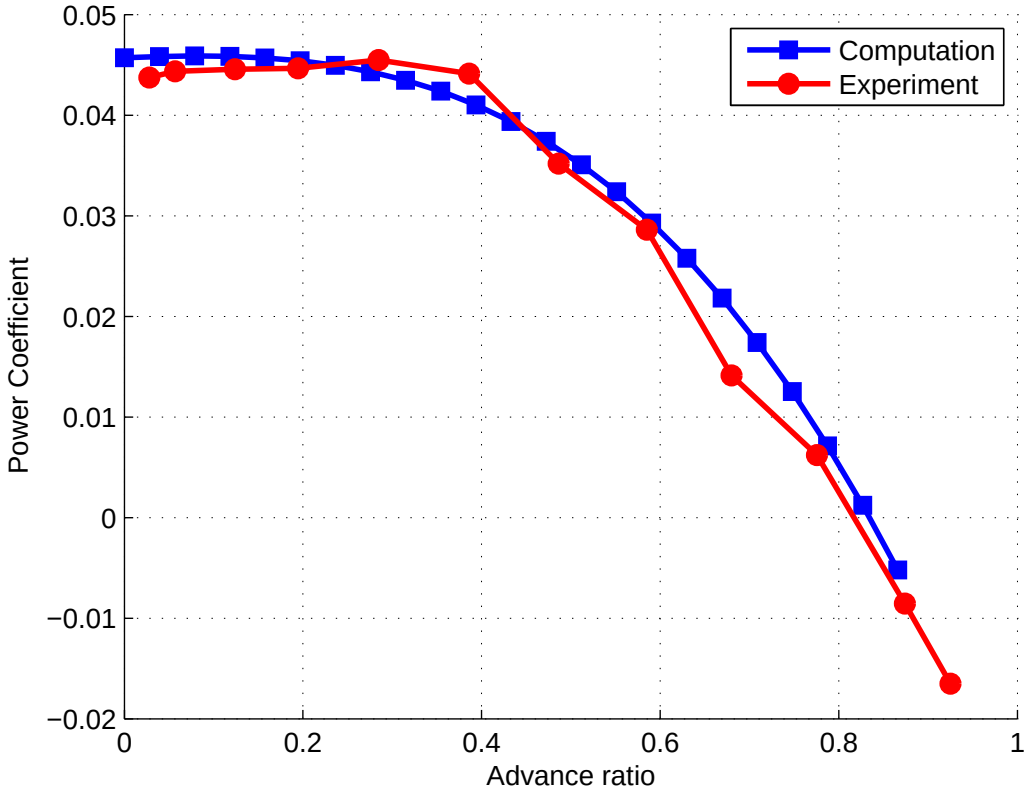

Figure 3.9: Propeller power estimation of APC 10x7E.

3.3 Stochastic Thrust Model and Validation

The stochastic thrust model is developed based on the measurement errors from the sensors used in the UAV application. A Monte Carlo simulation is used in developing the stochastic model. The uncertainties of the model come from three sources: forward speed measurement by pitot-static system, the propeller rotational speed measurement, and blade geometry description. Each of these sources will be analyzed in separate Monte Carlo simulations. The error in blade geometry description is a measure of how close is the aerodynamic model with the actual propeller aerodynamics and this error can be expressed as the error in the pitch angle and the lift curve slope. The models of

the uncertainties are drawn from a zero-mean Gaussian noise with certain variance.

Two Monte Carlo simulations are conducted for sensor measurement error. The first case is a simulation where the error is for the forward speed measurement and the errors are drawn from a normal distribution with 0.5 m/s, 1 m/s and 2 m/s standard deviations, respectively. The second case is for the rotational speed measurement error and the values of the error are also drawn from a normal distribution with 50 rpm and 100 rpm standard deviations. The third case of the simulation is a simulation where the error is from the blade geometry which includes the error in pitch and lift curve slope. The pitch uncertainties are 1° and 2°, respectively. The uncertainty in airfoil lift curve slope is represented by the percentage of the nominal value which is also drawn from a normal distribution with standard deviations of 0.05 and 0.15.

3.3.1 Velocity Uncertainty Effect

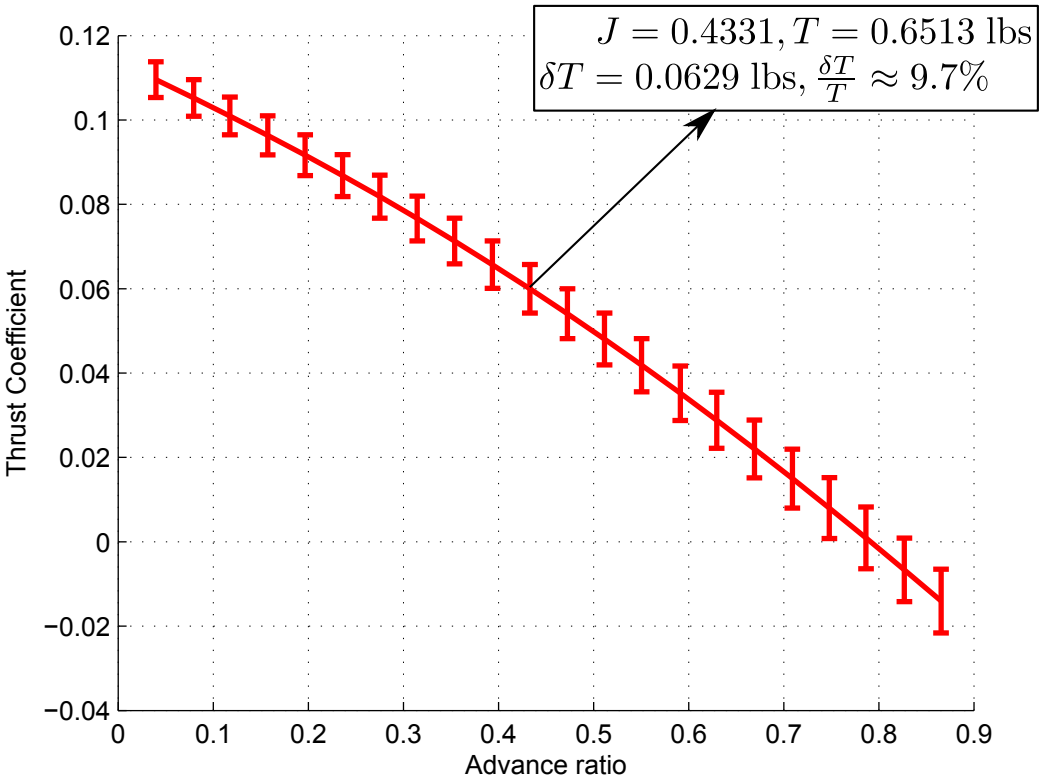

Figure 3.10: Thrust simulation result with forward velocity error of 1 m/s

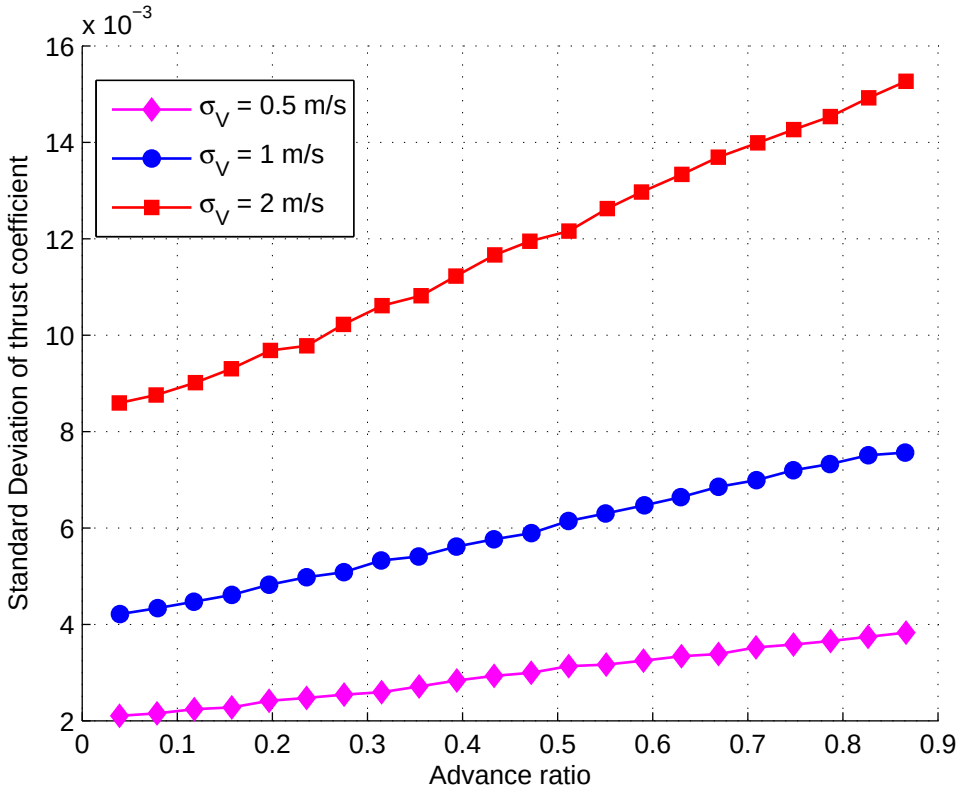

Figure 3.11: Error variation in thrust with advance ratio

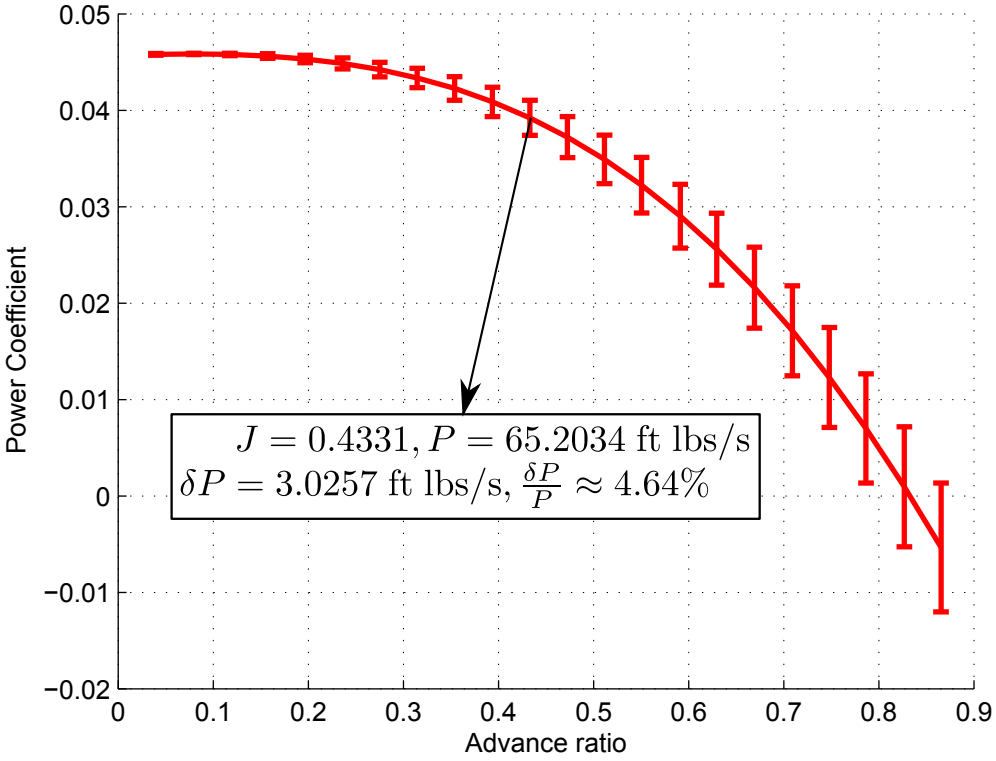

Figure 3.12: Power simulation result with forward velocity error of 1 m/s

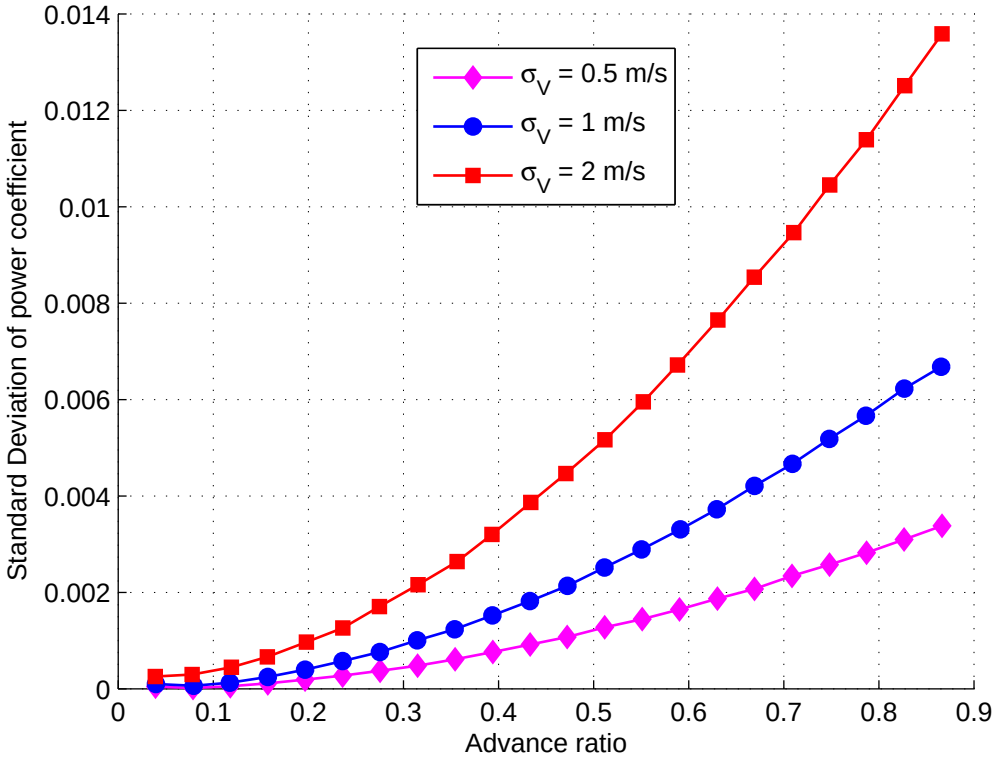

Figure 3.13: Error variation in power with advance ratio

The simulation results of forward velocity error are shown in Fig. 3.10 through Fig. 3.13. The error drawn from $N(0, (1 \text{ m/s})^2)$ has a significant effect to the thrust predicted as shown by the error bar of Fig. 3.10. Figure 3.11 shows that the thrust coefficient error increases as the advance ratio increases. The thrust coefficient error is proportional to the forward velocity error. It is also linear in advance ratio for small σ_V. The power coefficient error increases as the advance ratio increase and its increment is non-linear as shown by Fig. 3.12 and Fig. 3.13. The power coefficient error is proportional to the forward velocity error.

3.3.2 Rotational Speed Uncertainty Effect

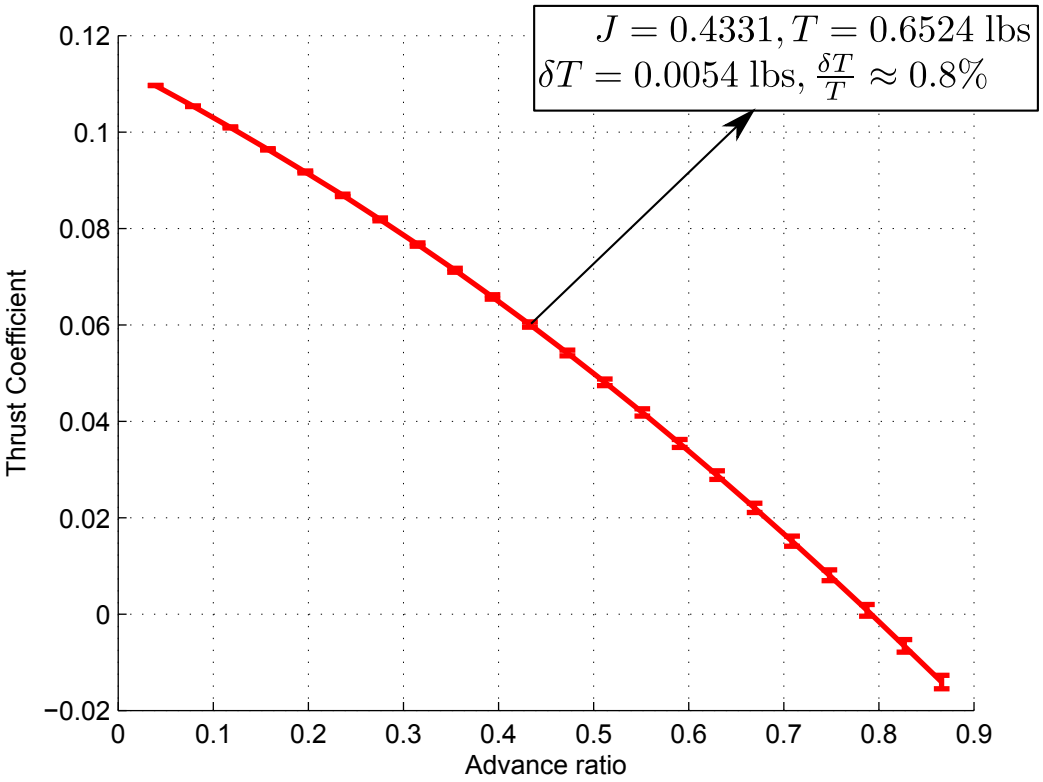

Figure 3.14: Thrust simulation result with rotational speed error of 50 rpm

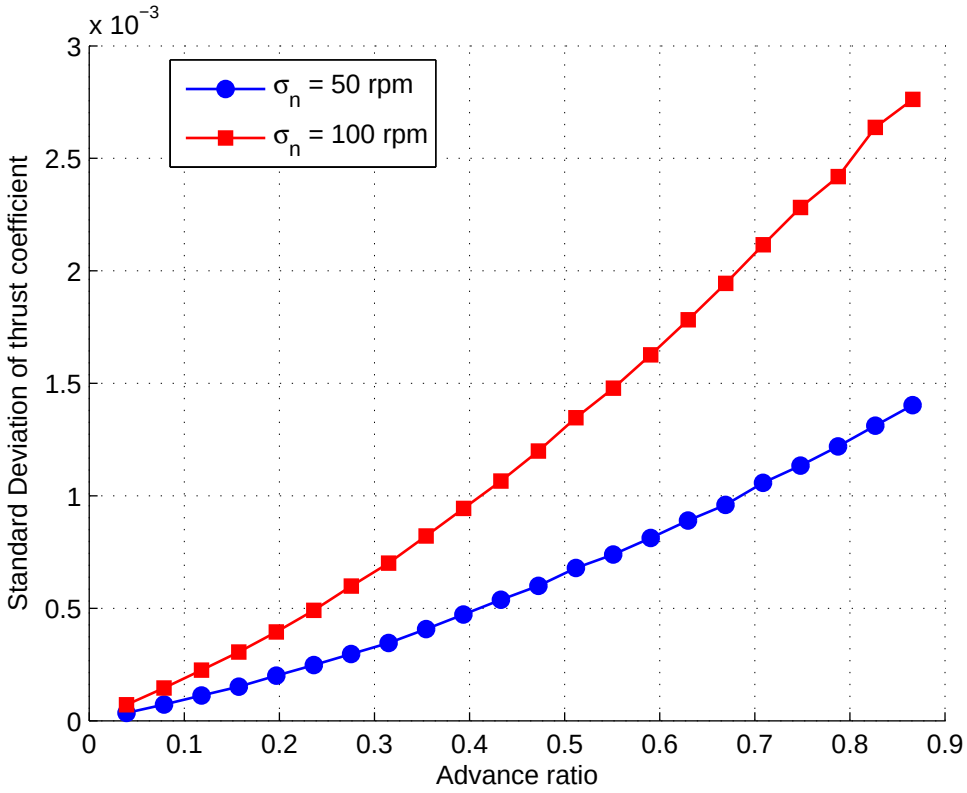

Figure 3.15: Error variation in thrust with advance ratio

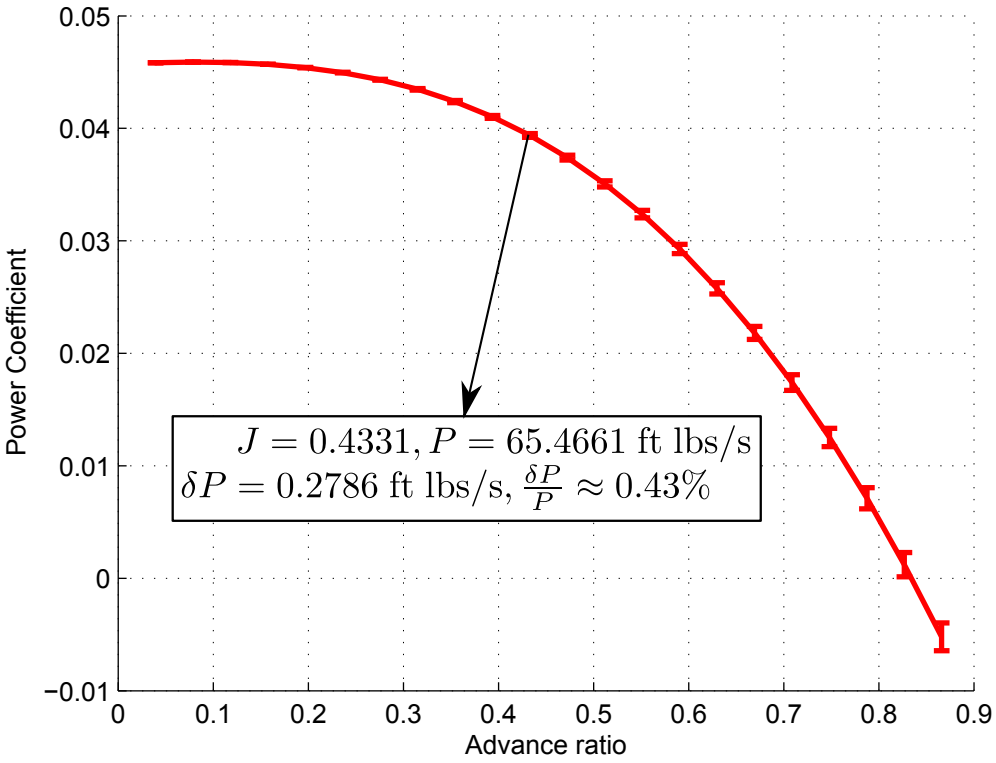

Figure 3.16: Power simulation result with rotational speed error of 50 rpm

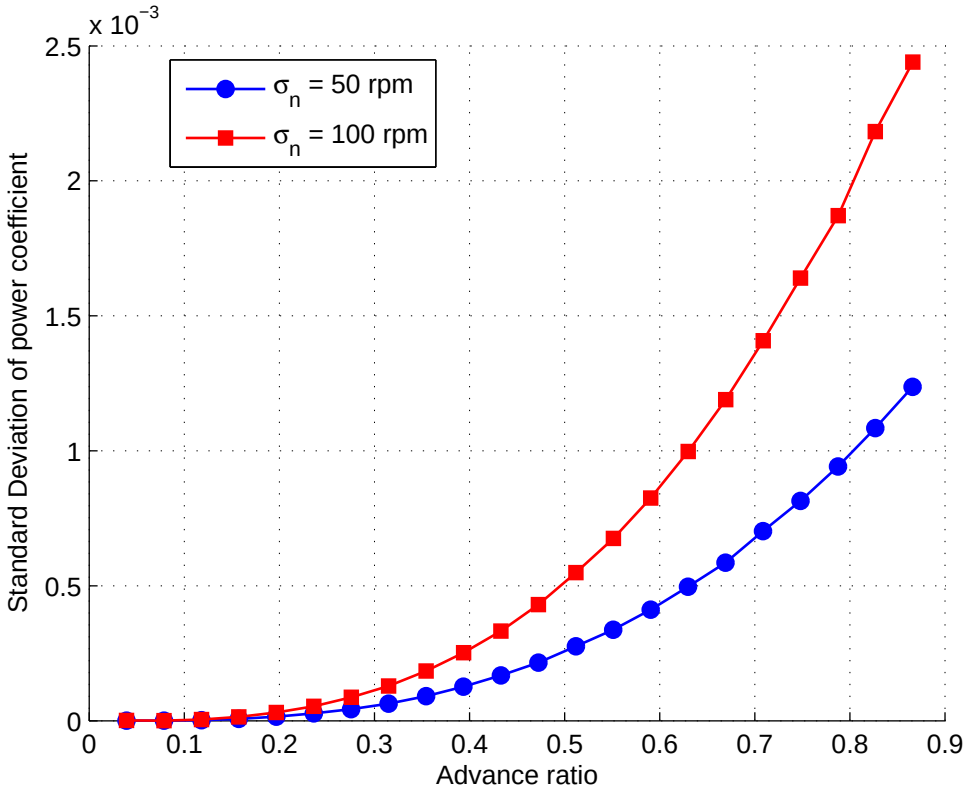

Figure 3.17: Error variation in power with advance ratio

Figures 3.14 to 3.17 show the simulation results for rotational speed error. The rotational speed error in this case drawn from $N(0, (50 \text{ rpm})^2)$ does not affect the results significantly as shown by Fig. 3.14 and Fig. 3.16. For this case, the error is small and negligible. Figures 3.15 and 3.17 show that the thrust and power coefficient errors increase as the advance ratio increases, respectively. The thrust and power coefficient error are proportional to the rotational speed error and non-linear with advance ratio.

3.3.3 Propeller Aerodynamic Uncertainty Effects

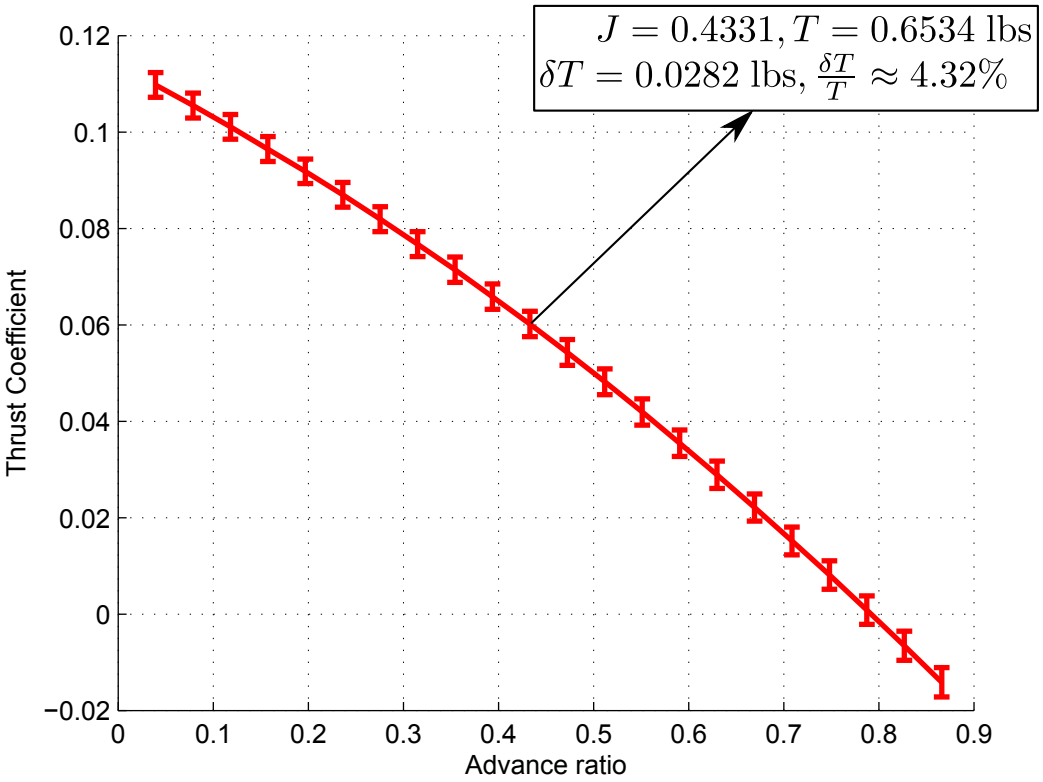

Figure 3.18: Thrust simulation result with pitch angle error of 2°

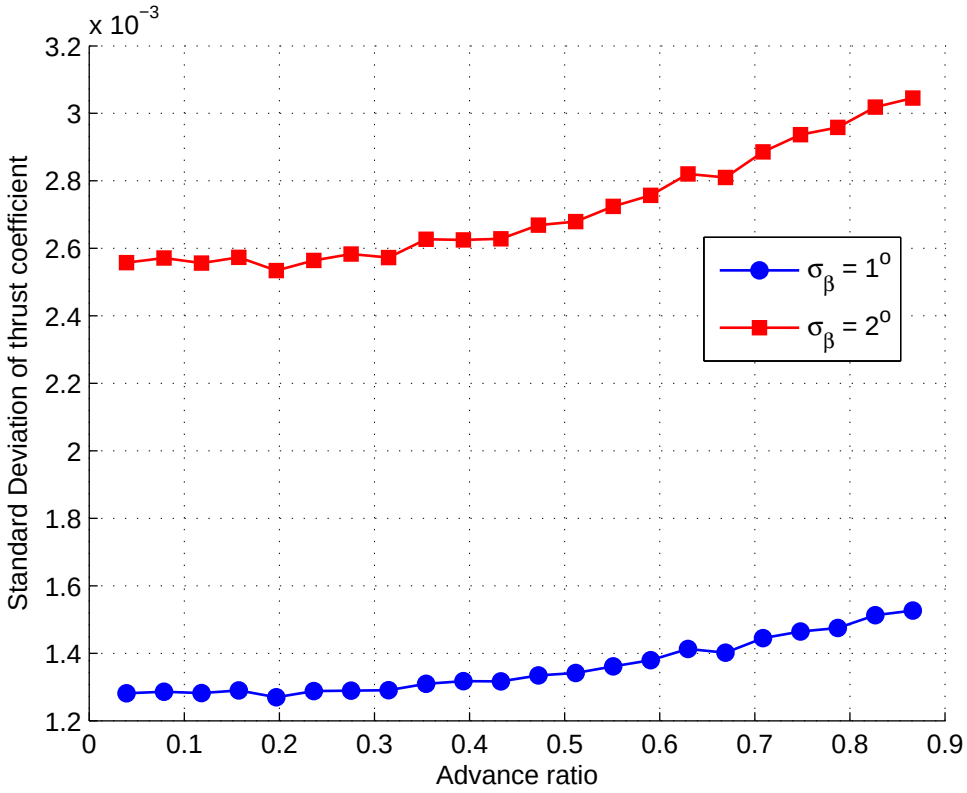

Figure 3.19: Error variation in thrust with advance ratio

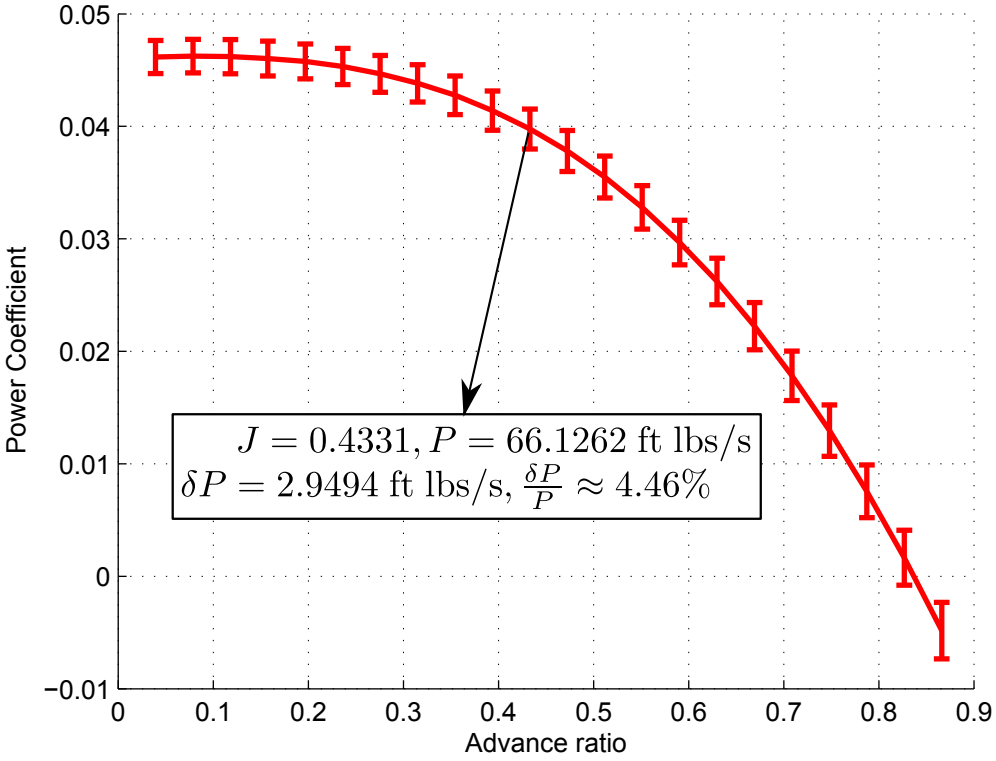

Figure 3.20: Power simulation result with pitch angle error of 2°

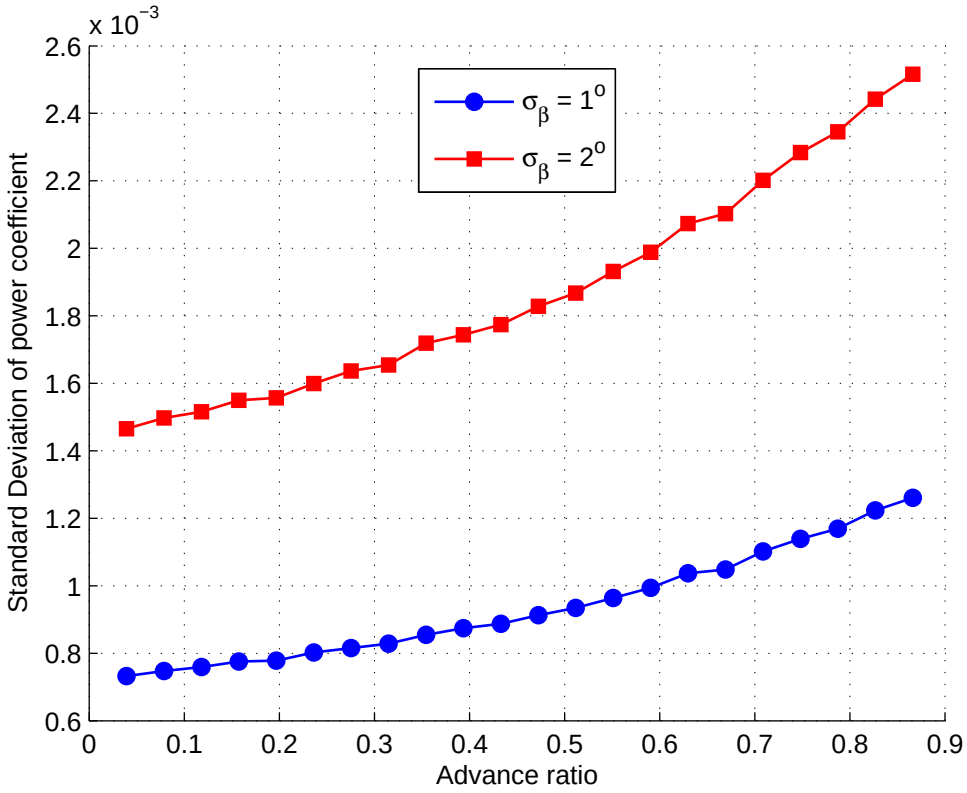

Figure 3.21: Error variation in power with advance ratio

The first of the propeller description errors is that of propeller pitch which is related to the propeller twist angle. Any perturbation in this pitch angle will directly affect the blade aerodynamic coefficients because the error will perturb the local angle of attack. The simulation results of pitch angle error are shown in Fig. 3.18 through Fig. 3.21. The error used in this case is $N(0,\ (2^{\circ})^2)$. This is seen to affect the result significantly as shown by the error bars of Fig. 3.18 and Fig. 3.20. Figures 3.19 and 3.21 show that the thrust and power coefficient errors increase as the advance ratio increases but the increment with respect to advance ratio is not as fast as the previous cases. The thrust and power coefficient errors are also proportional to the pitch angle error but non-linear in advance ratio.

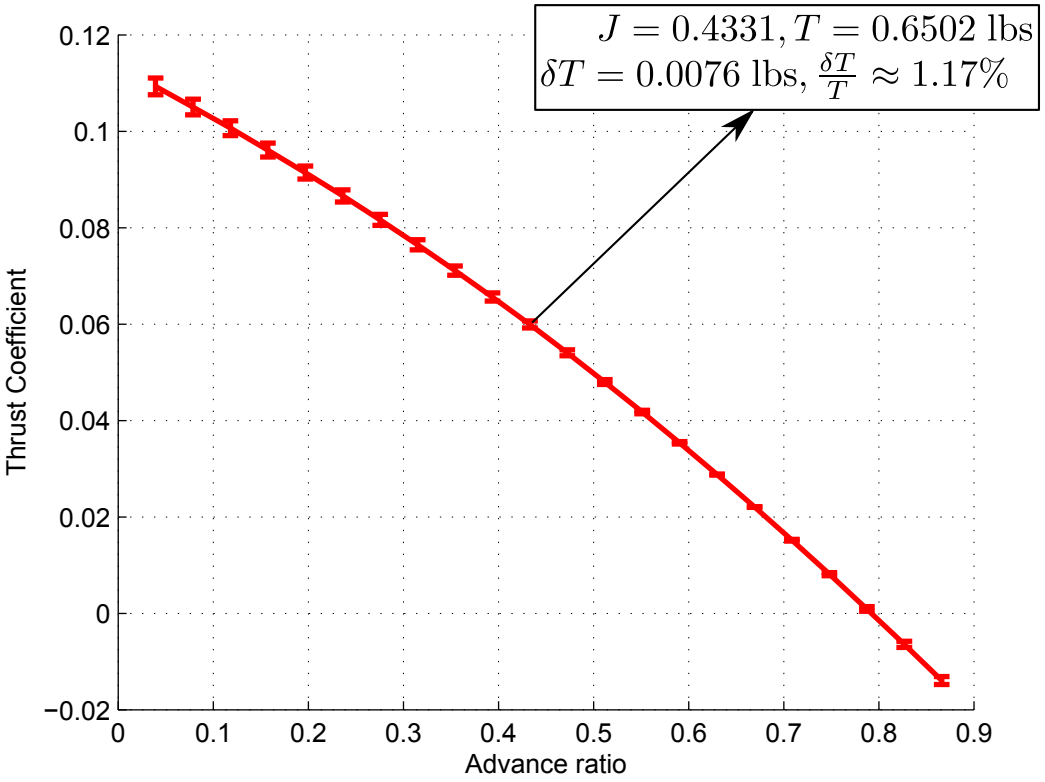

Figure 3.22: Thrust simulation result with lift curve slope error of 15%

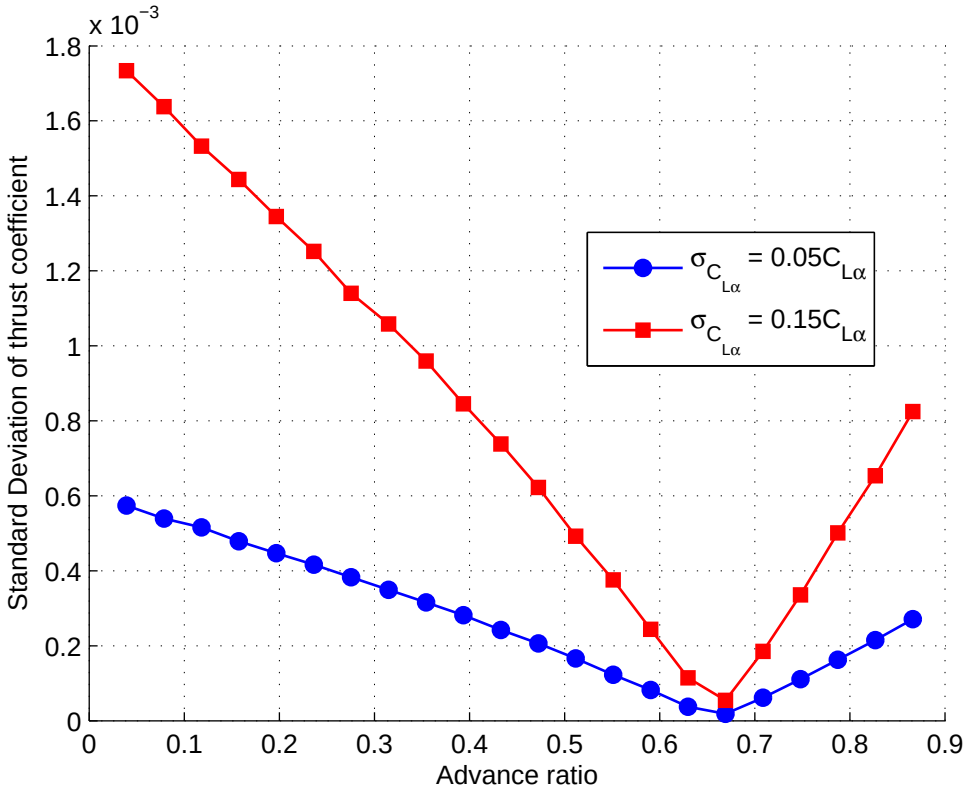

Figure 3.23: Error variation in thrust with advance ratio

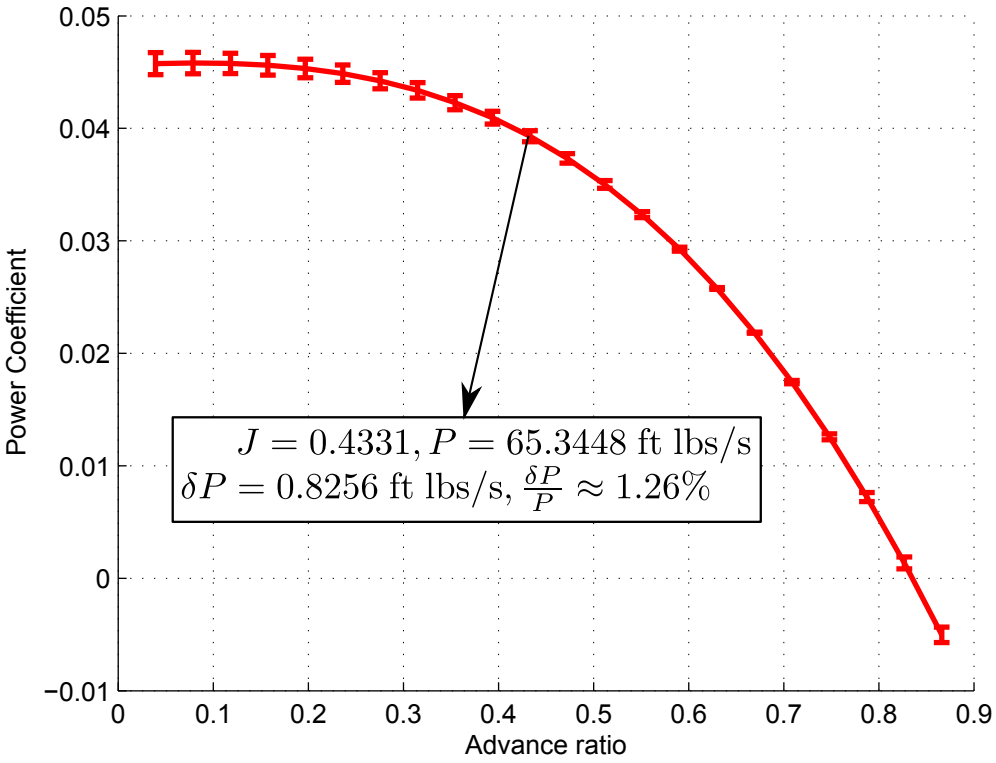

Figure 3.24: Power simulation result with lift curve slope error of 15%

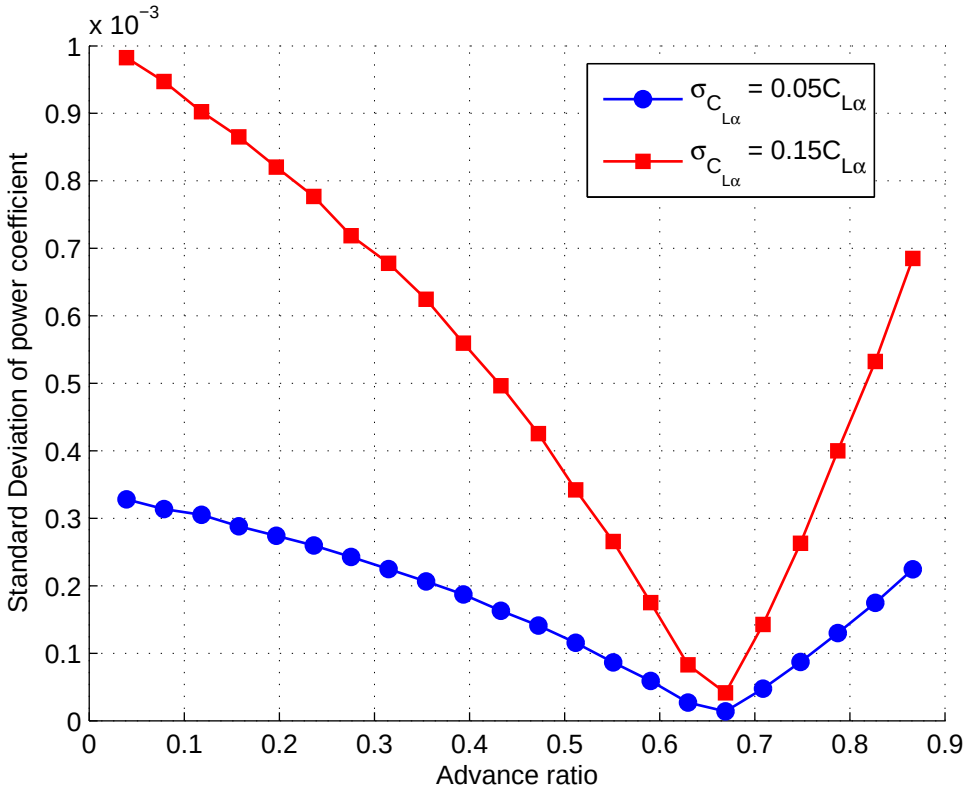

Figure 3.25: Error variation in power with advance ratio

The lift curve slope error is used to model the cross sectional error since the blade cross sections are represented by some known airfoils. The error of $N(0,\ (0.15C_{L_\alpha})^2)$ does not affect the result significantly as shown in Fig. 3.22 and Fig. 3.24. The error is very small and negligible for this case. Figures 3.23 and 3.25 show that the thrust and power coefficient errors decreases and then increases as the advance ratio increases, respectively. The reason for this trend of result is shown by Fig. 3.6 and Fig. 3.7. As the advance ratio increases, the sectional thrust coefficient decreases and becomes negative at certain advance ratio. The turning point of the thrust and power coefficient errors are the points when the thrust produced and the power required by the propeller are have local angle of attack around zero. Since the lift is modeled as a linear equation, the lift coefficient becomes constant as the angle of attack is near zero. This simulation

result shows that this type of error can be neglected if the actual blade cross section is known and well modeled.

Chapter 4

Stochastic Model of Aircraft Dynamics

Aircraft dynamics is a term used to describe the aircraft's behaviour in flight and its mathematical representation are the equations of motion. These equations of motion consist of aerodynamic coefficients, stability and control derivatives. As stated in the beginning of this thesis, the aircraft's equations of motion can be empirically determined by using a computational software, such as DATCOM[7]. To get more accurate aircraft dynamics, wind tunnel experiments are required for determining the parameters in the aircraft's equations of motion. This chapter explores the wind tunnel experiment on a small UAV (Mini-Ultrastick) and developing its stochastic aircraft dynamic model based on measurement errors.

4.1 Wind Tunnel Experiment

In general, the objective of this wind tunnel experiment is to determine the aircraft's aerodynamics. The parameters in aircraft's equations of motion can be computed using the experiment results. In this case, this experiment is performed using the closed-return wind tunnel facility at the University of Minnesota. This wind tunnel has a 40×60 inches test section. It is powered by 100 HP frequency controlled variable speed electric motor with P-38 Feathering Propeller. It is equipped with a six degree of freedom force balance (sting) to measure three axes of forces and moments. A pitot

probe for measuring airspeed is mounted at the beginning of the test section. The air pressure information is coming from a pressure server. The angle of attack is measured by an inclinometer. All of these outputs are processed by a data acquisition computer.

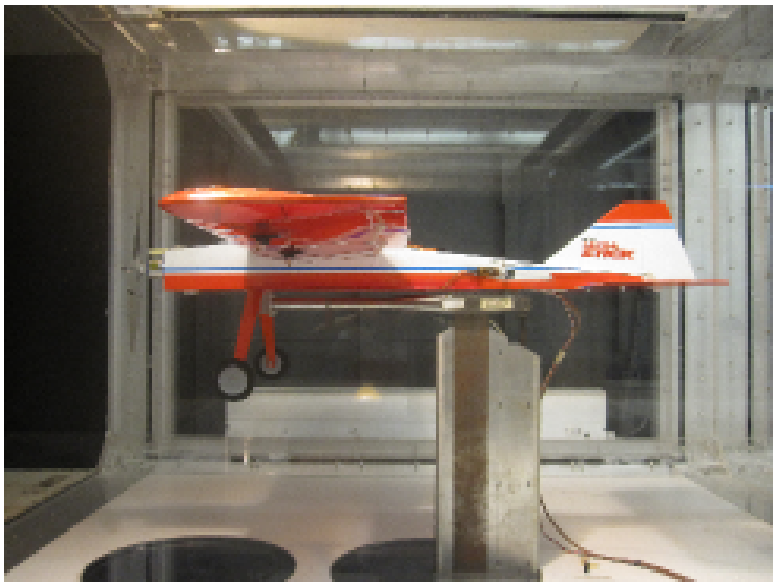

Figure 4.1: Mini-Ultrastick inside wind tunnel test section.

A small UAV (Mini-Ultrastick) is mounted on the sting inside the test section as shown in Fig. 4.1. This UAV has four control surfaces controlled by servos (ailerons, elevator, rudder, and flaps). In this experiment, there are only two control surfaces being used; elevator and rudder. Each control surface will only be deflected at its maximum, neutral, and minimum deflections. The deflection limits of elevator and rudder are $\pm 18^\circ$ and $\pm 30^\circ$, respectively. This experiment is performed such that there is only one control surface being deflected at each data acquisition. The angle of attack is varied form -10° to 22°. The tunnel speed is set at a constant speed of 8 m/s. The center of force and moment measurements are located and the sting's moment center (MC) as shown in Fig. 4.2. Since the measurement center of interest is the aircraft's center of gravity (CG), all of the measurements will be transferred from MC to CG.

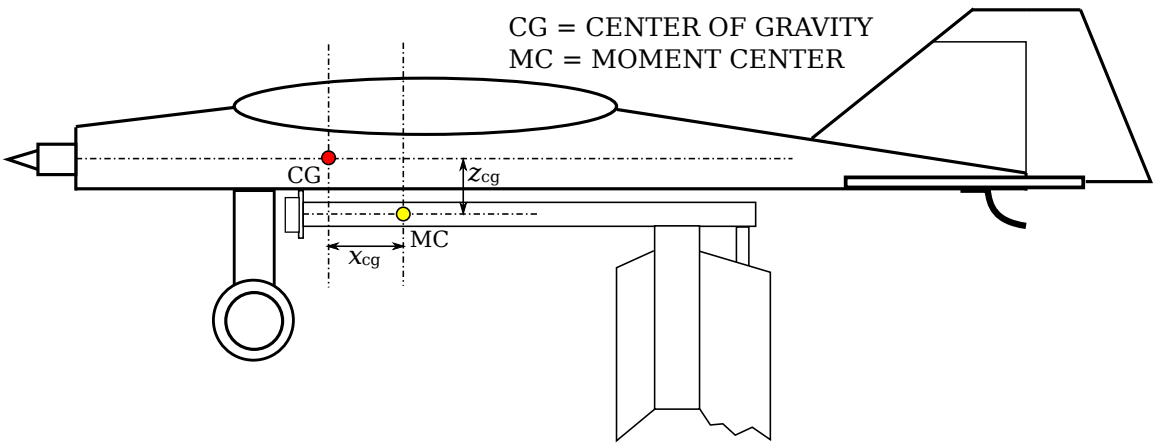

Figure 4.2: Mini-Ultrastick's center of gravity and moment center.

4.2 Experiment Results

The experiment was performed eleven times such that there are eleven sets of data collected as shown in Fig. 4.3 and Fig. 4.4 for the tunnel speed and air density variation, respectively. The tunnel's air speed varies with the angle of attack while the air density is constant during the experiment. The variation of the air speed measurement is caused by the changing in frontal area of the aircraft as the angle of attack was varied which, in turn, changes the degree to which the tunnel cross section is blocked. As shown in Fig. 4.3, the air speed is maximum about zero angle of attack and this condition represents the smallest frontal area of the aircraft as seen by the airflow. The air speed decreases as the frontal area increases. This result is caused by the fact that the wind tunnel test section is too small for this small UAV.

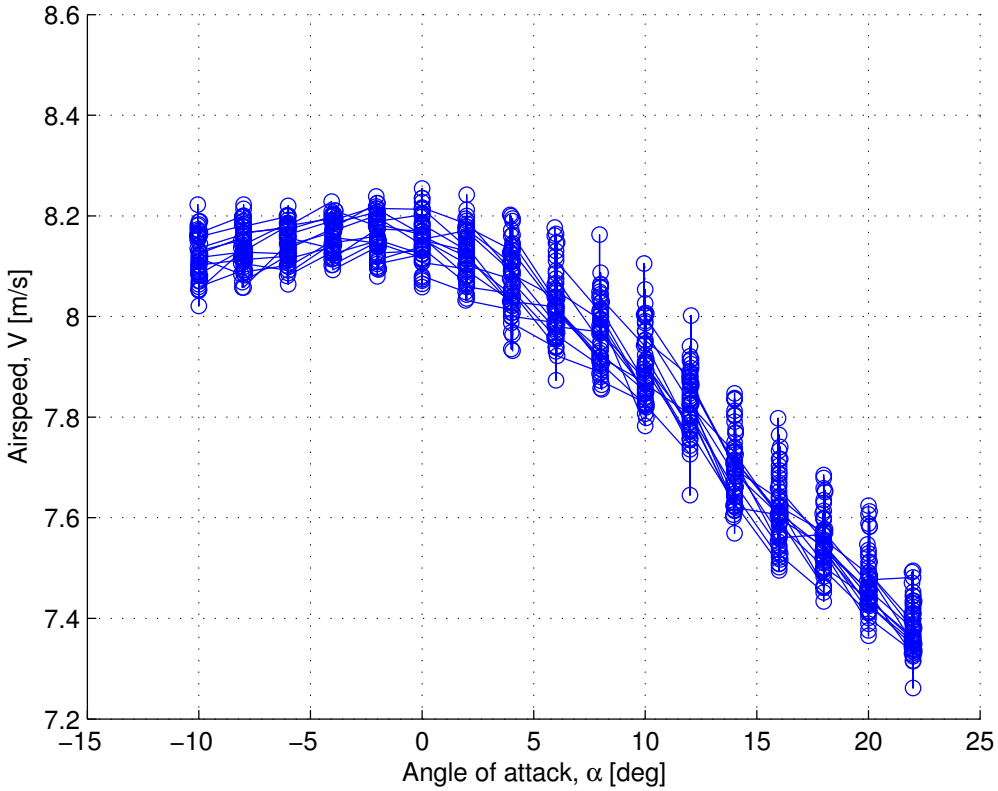

Figure 4.3: Wind tunnel speed measurements.

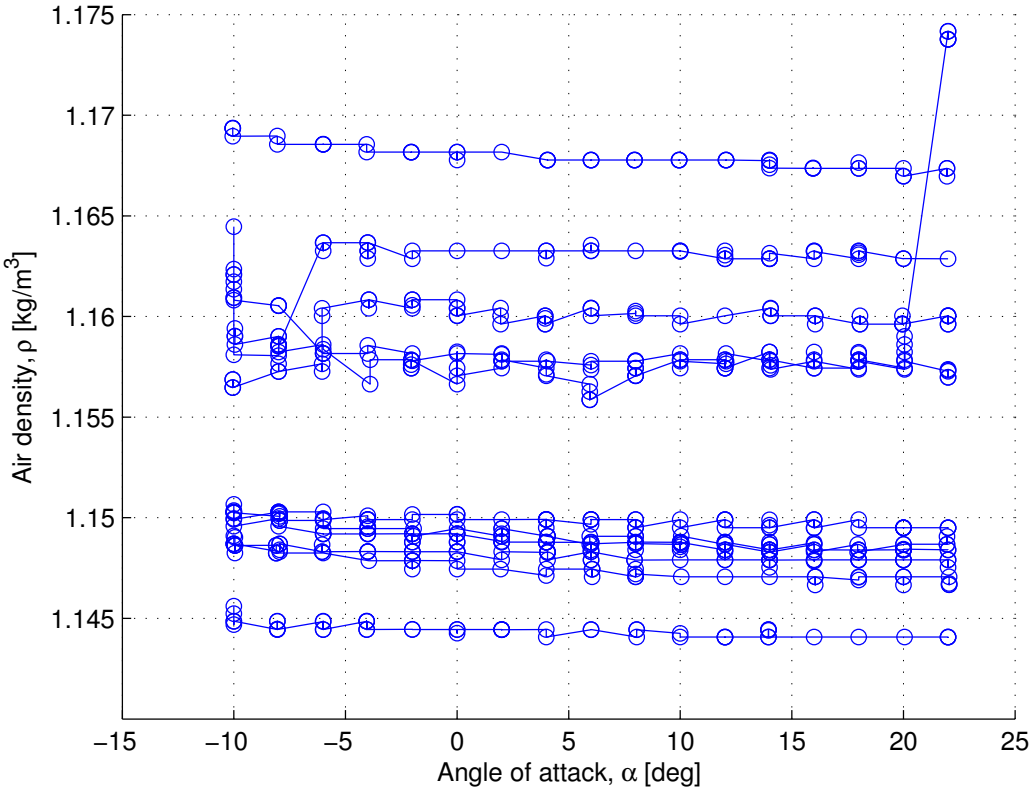

Figure 4.4: Wind tunnel air density measurements.

The aerodynamic coefficients are computed by combining these eleven set of data based on their measurement errors. The wind tunnel measurement errors are shown in Appendix B. The standard deviation values are used in merging the data through a

linearized filter. The aerodynamic equations used in data reduction are shown below:

$$D = -F_X \cos\alpha - F_Z \sin\alpha = \frac{1}{2}\,\rho\,V^2\,S_w\,C_D \tag{4.1}$$

$$Y = F_Y = \frac{1}{2}\,\rho\,V^2\,S_w\,C_Y \tag{4.2}$$

$$L = F_X \sin\alpha - F_Z \cos\alpha = \frac{1}{2}\,\rho\,V^2\,S_w\,C_L \tag{4.3}$$

$$L_{cg} = M_X - z_{cg}\,F_Y = \frac{1}{2}\,\rho\,V^2\,S_w\,b_w\,C_l \tag{4.4}$$

$$M_{cg} = M_Y + z_{cg}\,F_X = \frac{1}{2}\,\rho\,V^2\,S_w\,c_w\,C_m \tag{4.5}$$

$$N_{cg} = M_Z + x_{cg}\,F_Y = \frac{1}{2}\,\rho\,V^2\,S_w\,b_w\,C_n \tag{4.6}$$

The experiment results for elevator deflection are plotted from Fig. 4.5 to Fig. 4.10. This elevator deflection affects the lift and the pitching moment of the aircraft. A positive elevator deflection causes an increase in lift and a decrease in pitching moment while a negative one will do the opposite as shown in Fig. 4.7 and Fig.4.9 for lift coefficient and pitching moment coefficient, respectively. The plots of drag coefficient and pitching moment coefficient clearly show when the aircraft enters into stall condition. The drag coefficient shows that there is a sudden increase in drag between angle of attack of 12° and 14° as shown in Fig. 4.5. This trend also can be seen in Fig. 4.9. The stall region is also marked by the high standard deviation values as shown by the y-axis error bar.

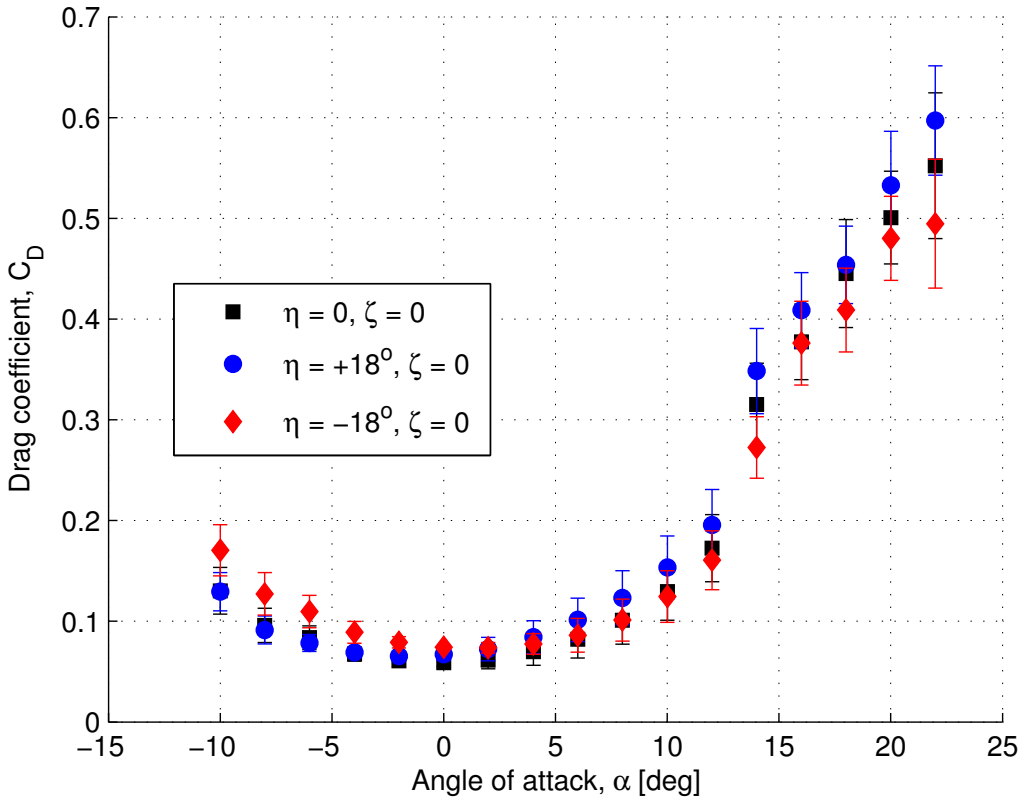

Figure 4.5: Drag coefficient for elevator deflection.

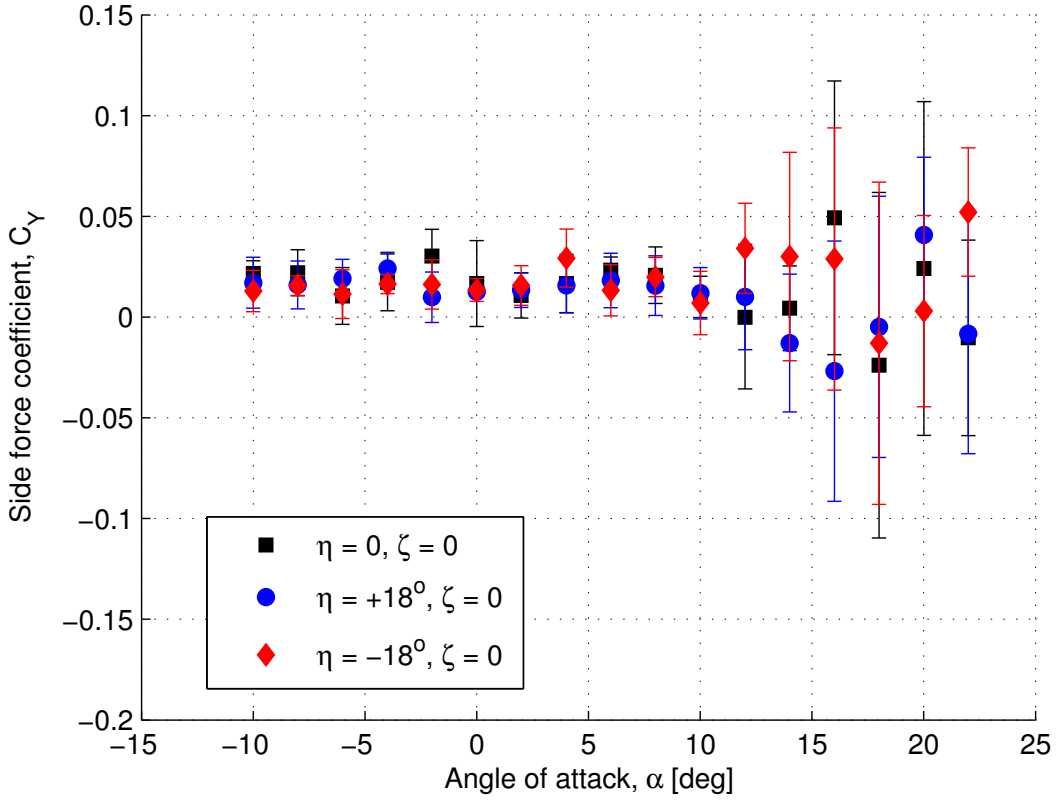

Figure 4.6: Transverse force coefficient for elevator deflection.

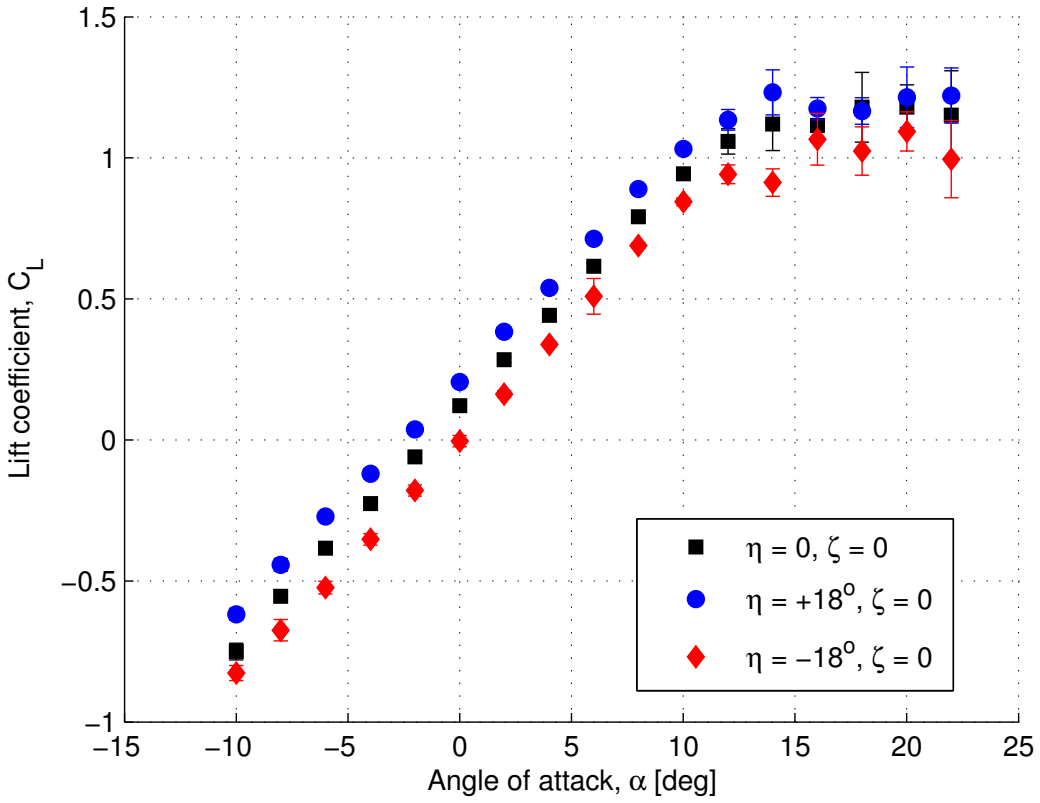

Figure 4.7: Lift coefficient for elevator deflection.

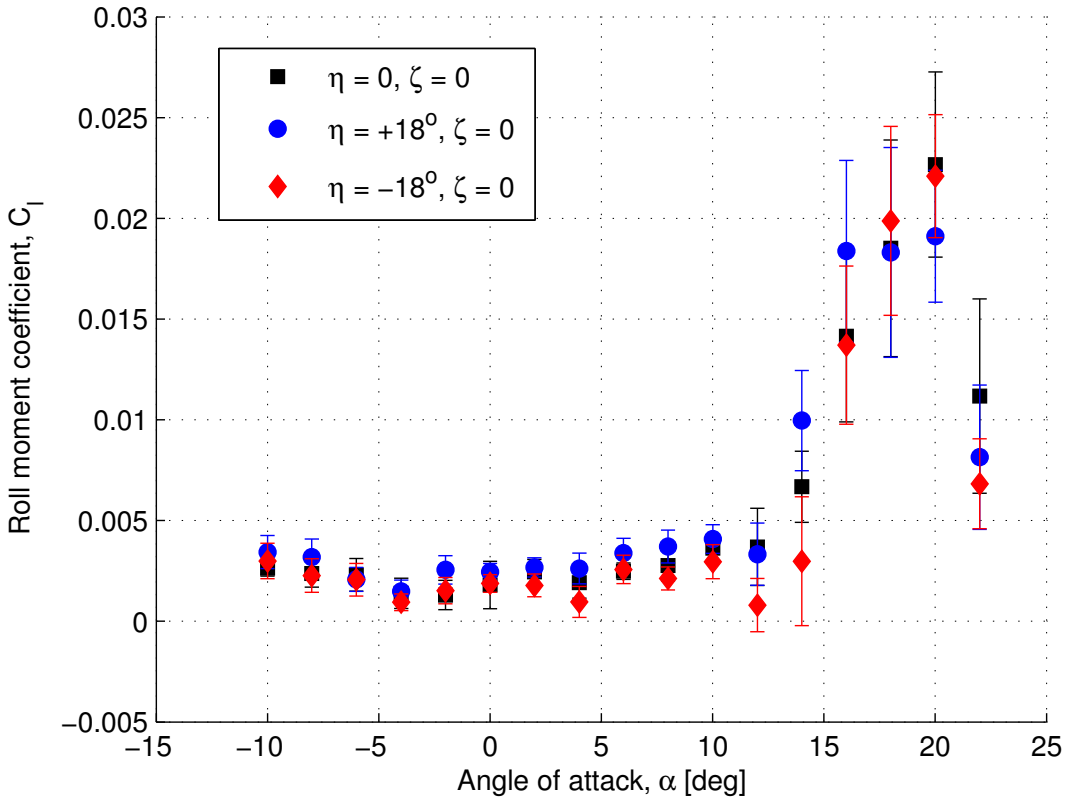

Figure 4.8: Rolling moment coefficient for elevator deflection.

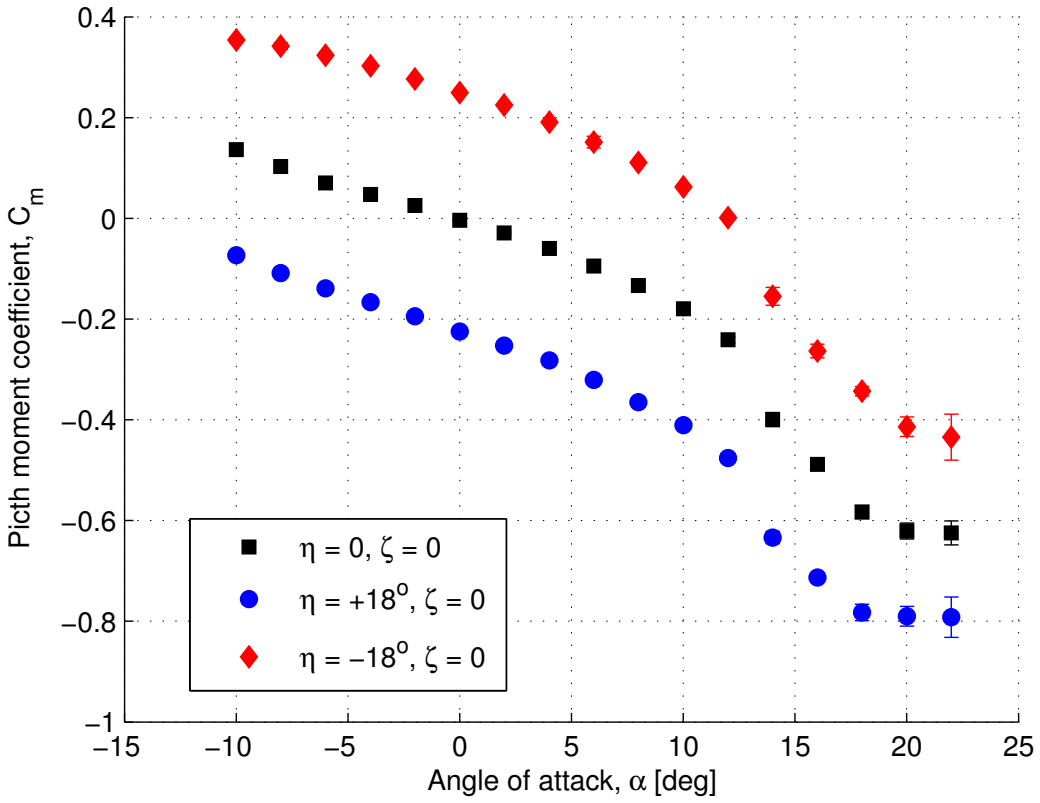

Figure 4.9: Pitching moment coefficient for elevator deflection.

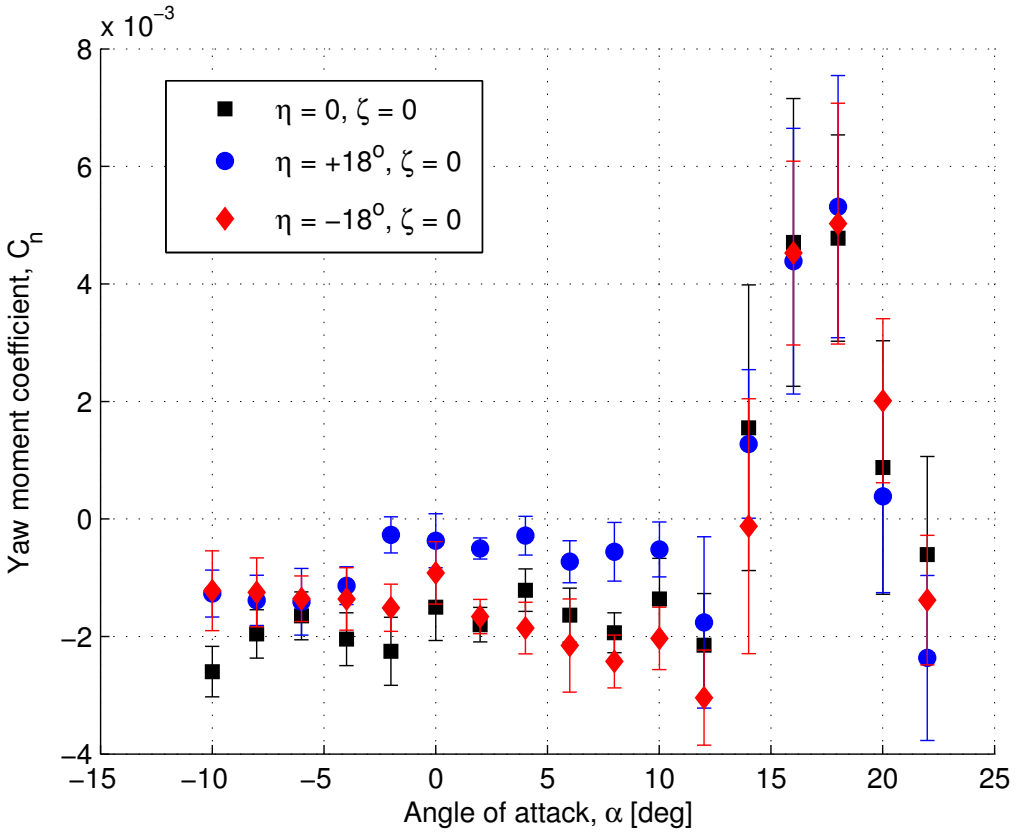

Figure 4.10: Yawing moment coefficient for elevator deflection.

Figure 4.11 to Fig.4.16 show the experiment results for rudder deflection. This rudder deflection will affect the side force balance. A positive rudder deflection gives a positive side force and a negative the yawing moment of the aircraft as shown in Fig. 4.12 and Fig. 4.16, respectively. The rudder deflection will not affect the lift and pitching moment as the elevator does. The rudder effectiveness is affected by the angle of attack. The frontal area seen by the airflow increases as the angle of attack increases and this will block the airflow to flow through the rudder. The rudder becomes dramatically less effective in the stall region as shown in Fig. 4.16. This set of data also shows that the stall region begins at the angle of attack between 12° and 14°.

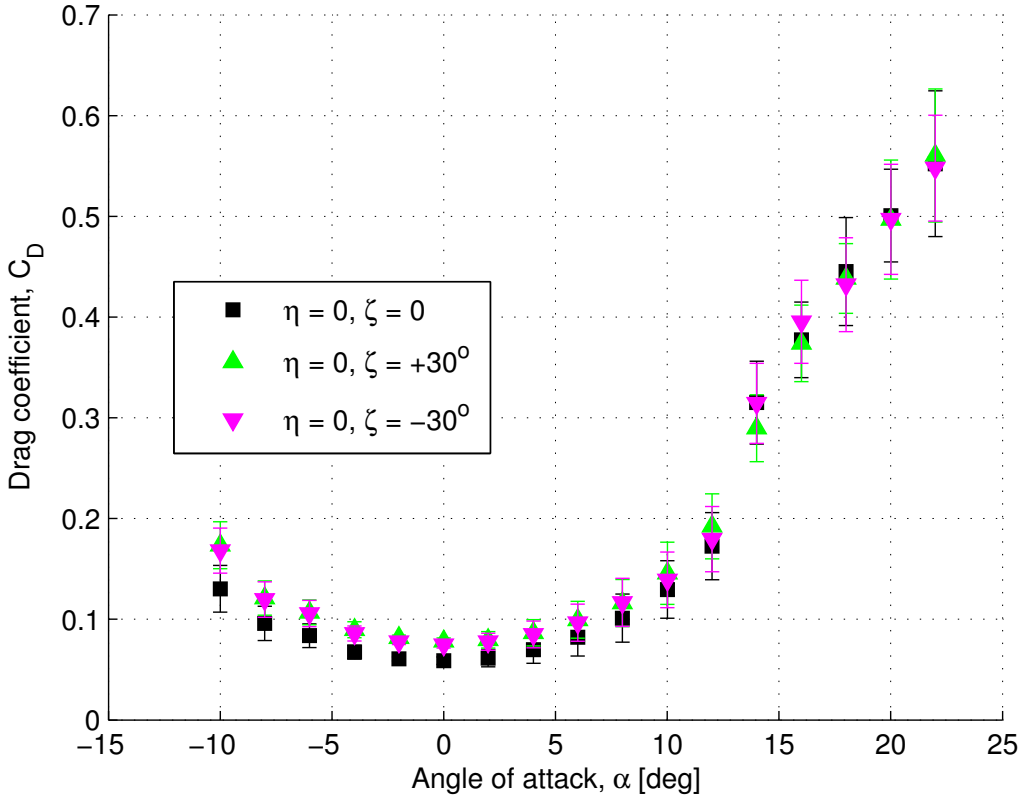

Figure 4.11: Drag coefficient for rudder deflection.

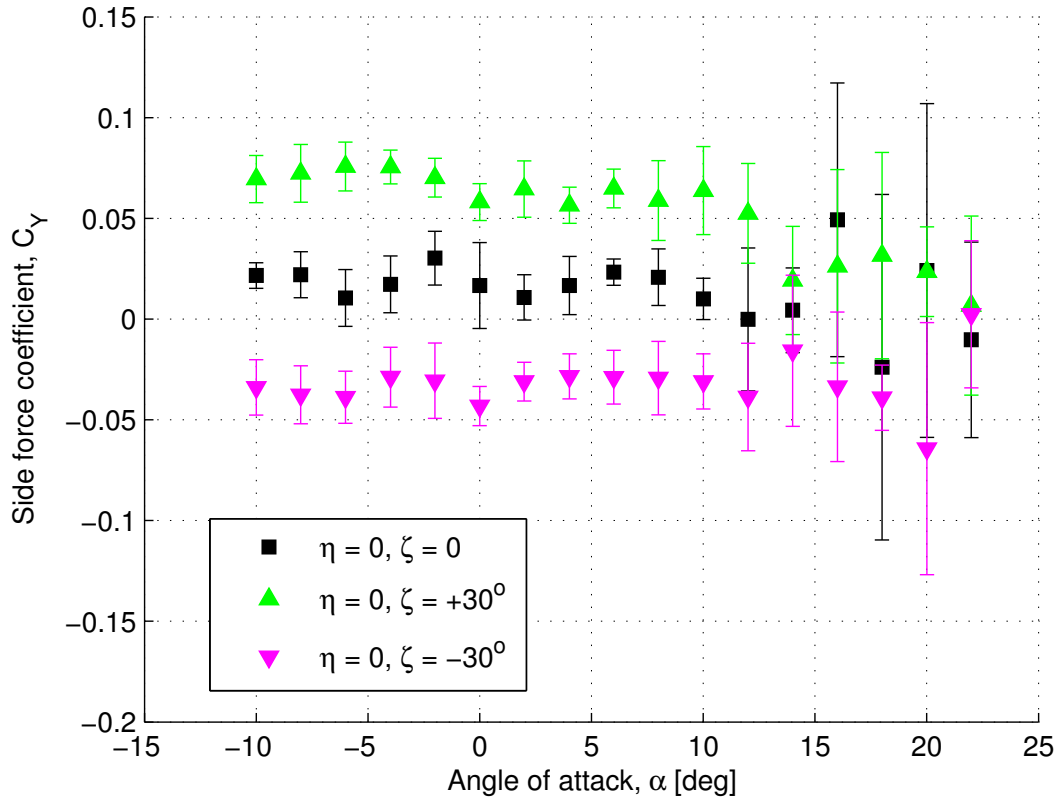

Figure 4.12: Transverse force coefficient for rudder deflection.

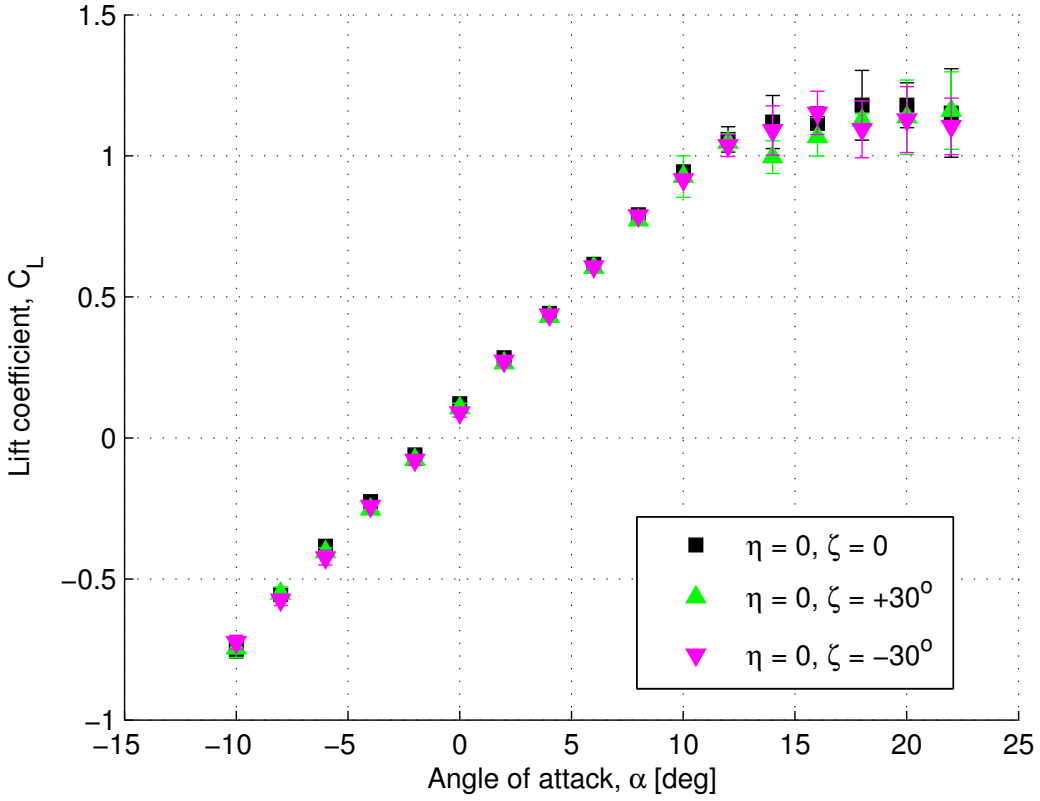

Figure 4.13: Lift coefficient for rudder deflection.

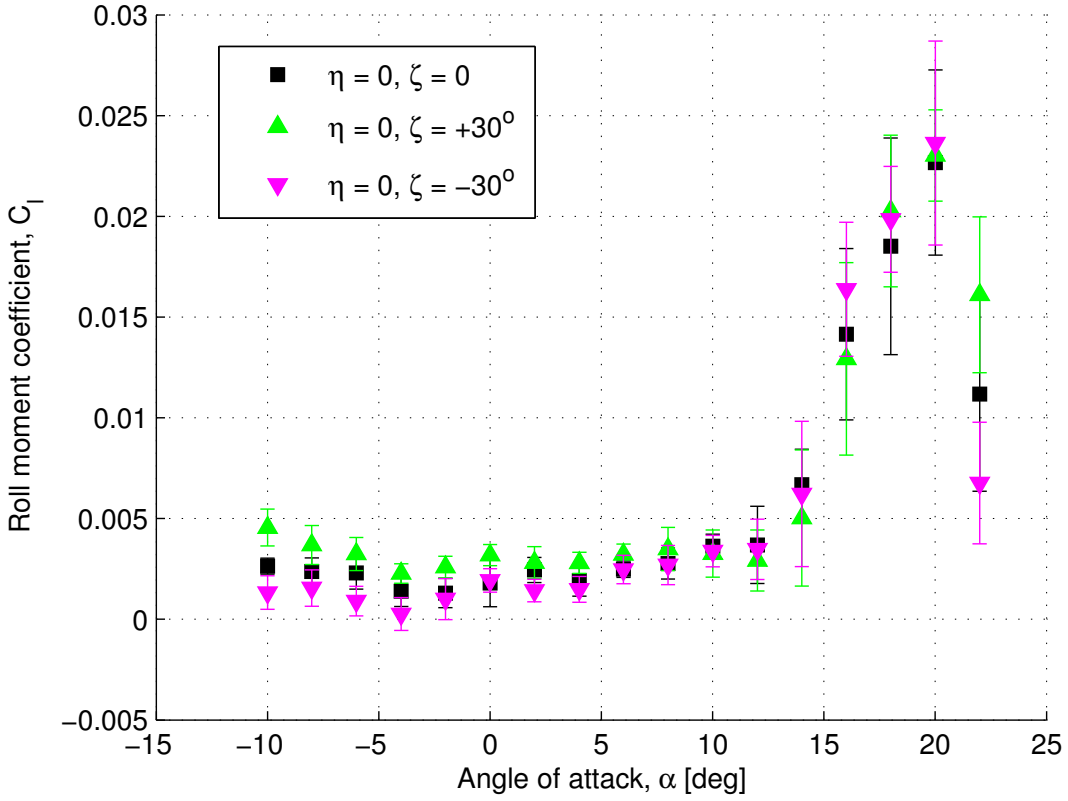

Figure 4.14: Rolling moment coefficient for rudder deflection.

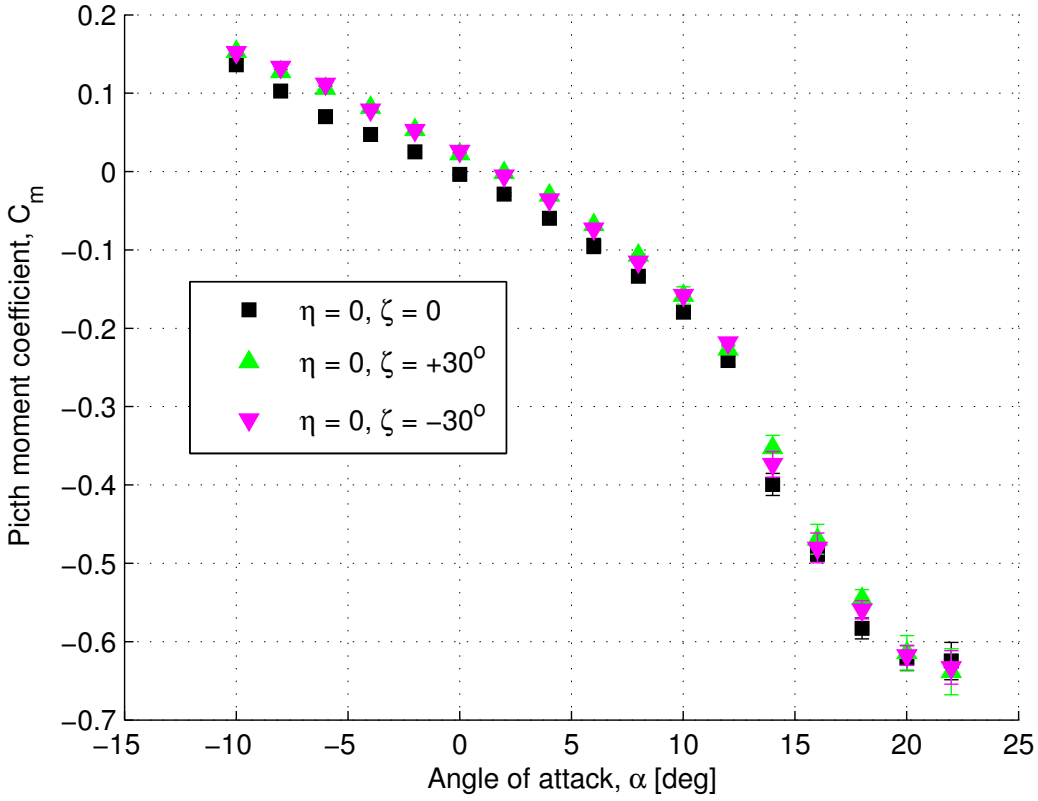

Figure 4.15: Pitching moment coefficient for rudder deflection.

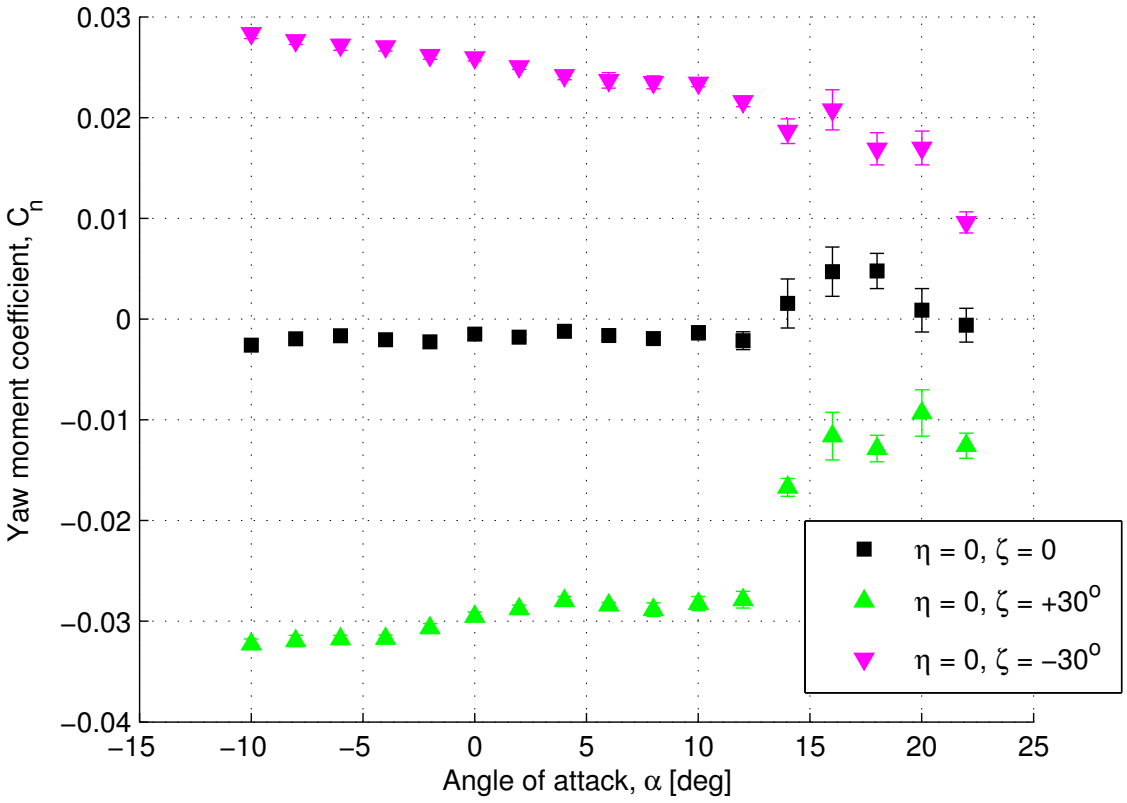

Figure 4.16: Yawing moment coefficient for rudder deflection.

Chapter 5

Conclusions and Future Work

5.1 Conclusions

This thesis has shown the result of propeller performance estimator and model of wind tunnel uncertainties from a small UAV. The propeller performance estimator is based on the Blade-element and Momentum theory with the induced angle of attack or the induced velocity computed by combining the Goldstein's vortex theory and Kutta-Joukowski theorem. The stochastic model of propeller performance was developed by perturbing the parameters which describe the operating conditions and propeller geometry. The objective was to see how the propeller performance is affected by the uncertainties in velocity, RPM, propeller geometry and aerodynamics. The model of wind tunnel uncertainties was developed based on the experiment of a small UAV (Mini-Ultrastick) in wind tunnel. The objective of this experiment is to see how the uncertainties of the aerodynamic coefficients varies with the angle of attack.

From the results of propeller performance prediction, the nominal performance result agrees with the experimental result. In the stochastic model, the results showed that in general the uncertainties in predicted thrust increases as the advance ratio increases. The thrust and power coefficient uncertainties are proportional to the uncertainty of the inputs. However, for the case where the lift curve slope was perturbed, the uncertainties decreases and increases as the advance ratio varies from low to high.

In the wind tunnel experiment, the results showed that the uncertainties of the aerodynamic coefficients can split into two regions, before stall (low angle of attack)

and after entering stall (high angle of attack) conditions. The angle of attack that splits these two regions is between 12° and 14°. The aerodynamic coefficient curves showed that there is a discontinuity. The uncertainties are relatively small before stall and become large after entering the stall region.

5.2 Future Work

The following is a list of some areas for future work:

1. **Propeller blade's physical measurement and its aerodynamics**: Any propeller has its own blade geometry description which includes chord length, thickness, and pitch angle. The blade cross section is an airfoil and the blade will produce lift and drag when the propeller is in operation. The information about the blade geometry and its aerodynamics is crucial information in predicting the propeller performance. However, determining or predicting this information for any propeller is a hard problem unless the manufacturer provides one. It is very difficult to do reverse engineering to get this information. A method for doing this reverse engineering quickly will be beneficial.

2. **Considering the effect of compressible flow**: The propeller performance results in this thesis ware computed by assuming that the airflow is incompressible. The propeller blade sections near the tip normally or may operate at high subsonic speed and the airflow at this condition violates the assumption of the incompressible flow.

3. **Considering multiple sources of uncertainties in the propeller performance computation**: The uncertainty analysis performed in this thesis only looked at a single source of uncertainty.

4. **Modeling the boundary layer of the wind tunnel**: The result of the wind tunnel experiment of a small did not take into account the effect of boundary layer. The tunnel speed varies with the pitch angle or angle of attack.

References

[1] Hickman, M., P. Mirchandani, A. Angel and D. Chandnani, NCRST-F Year 1 Report. *Project 3 - Needs Assessment and Allocation of Imaging Resources For Transportation Planning and Management*, ATLAS Research Center, University of Arizona. Tucson, AZ, September 30, 2001.

[2] Gebre-Egziabher D., *RPV/UAV Surveillance for Transportation Management and Security*, University of Minnesota Intelligent Transportation Systems Institute Report CTS 08-27, Minneapolism MN, December 2008.

[3] Nonami, Kenzo, *Modeling and Control of Unmanned Small Scale Rotorcraft UAVs and MAVs*, SpringerLink, London, 2010.

[4] Weibel, R. E., R. J. Hansman, *Safety Considerations for Operation of Different Classes of UAV's in the NAS*, AIAA paper 2004-6244. Proceedings of the Aviation Technology, Integration and Operation (ATIO) Forum, Chicago, IL, September 2004.

[5] Weibel, R. E., R. J. Hansman, *An Integrated Approach to Evaluating Risk Mitigation Measures for UAV Operational Concepts in the NAS*, AIAA paper 2005-6957. Proceedings of Infotech Aerospace Conference. Arlington, VA, September, 2005.

[6] Gebre-Egziabher D., Z. Xing, *Analysis of Unmanned Aerial Vehicles Concepts of Operations in ITS Applications*, University of Minnesota Intelligent Transportation Systems Institute Report CTS 11-05, Minneapolis, MN, December 2011.

[7] DATCOM, `http://www.pdas.com/datcom.html`

[8] Raymer, Daniel P., *Aircraft Design: A Conceptual Approach*, 3th ed., AIAA Education Series, Virginia, 1999.

[9] Roskam, Jan, *Aircraft Design*, 3rd ed., DARcorporation, 2002.

[10] Watts, Henry C., *The Design of Screw Propellers for Aircraft.* Longmans, Green and Co., New York, 1920.

[11] Theodorsen, Theodore, *Theory of Propellers*, McGraw-Hill Book Company, New York, 1948.

[12] Weick, Fred. E., *Aerodynamic tests were made with four geometrically similar metal propellers of different diameters*, National Advisory Committee for Aeronautics, NACA TR No. 339, 1931.

[13] Weick, Fred. E., *Full-scale wind-tunnel tests on several metal propellers having different blade forms*, National Advisory Committee for Aeronautics, NACA TR No. 340, 1931.

[14] Freeman, Hugh B., *Comparison of full-scale propellers having R.A.F.-6 and Clark Y airfoil sections*, National Advisory Committee for Aeronautics, NACA TR No. 378, 1932.

[15] Hartman, Edwin P., David Biermann, *The aerodynamic characteristics of full-scale propellers having 2, 3, and 4 blades of Clark y and R.A.F. 6 airfoil sections*, National Advisory Committee for Aeronautics, NACA TR No. 640, 1938.

[16] McCormick, Barnes W., *Aerodynamics, Aeronautics and Flight Mechanics*, 2nd ed., Wiley, New York, 1995.

[17] Wald, Quentin R., *The Aerodynamics of Propellers*, Progress in Aerospace Science 42, Elsevier, 2006 (pages 85 - 128).

[18] Adkins, Charles N., Robert H. Liebeck, *Design of Optimum Propeller*, Jounal of Propulsion and Power, Vol. 10, No. 15, Sept. - Oct. 1994.

[19] Owens, D. Bruce, David E. Cox, Eugene A. Morelli, *Development of a Low-Cost Sub-Scale Aircraft for Flight Research: The FASER Project*, 25th AIAA Aerodynamic Measurement Technology and Ground Testing Conference, AIAA 2006-3306, San Francisco, California, June 2006.

[20] Mises, R., *Theory of Flight*. Dover, New York, 1945.

[21] Weick, Fred E., *Aircraft Propeller Design*. McGraw Hill, New York, 1930.

[22] Corson, Blake W., *A Review of Propeller Theory*, NACA: Univ. Conf. on Aerodyn., Jan 1, 1948.

[23] Bertin, John J. and Micheal L. Smith, *Aerodynamics for Engineers*, 3rd ed., Prentice-Hall Inc., New Jersey, 1998.

[24] Anderson, John D., *Fundamental of Aerodynamics*, 4th ed., McGraw-Hill, New York, 2007.

[25] Wind Tunnel of the Department of Aerospace Engineering and Mechanics, University of Minnesota, `http://www.aem.umn.edu/facilities/windtunnel/`

[26] APC Propellers (personal communication, April 5, 2011) `http://www.apcprop.com`

[27] Selig, Micheal S. and Gavin Ananda, *Low Reynolds Number Propeller Performance Data: Wind Tunnel Corrections for Motor Fixture Drag*, University of Illinois at Urbana-Champaign, 2011. `http://www.ae.illinois.edu/m-selig/props/uiuc-props-wind-tunnel-correction.pdf`

Appendix A

Nomenclature

A	Actuator disc area
B	Number of propeller blades
C_1	Total pressure in front of actuator disc
C_2	Total pressure in behind of actuator disc
C_D	Drag coefficient
C_L	Lift coefficient
$C_{L\alpha}$	Lift curve slope
C_P	Power coefficient
C_Q	Torque coefficient
C_T	Thrust coefficient
C_Y	Side force coefficient
C_{df}	Fixture drag coefficient
C_l	Rolling moment coefficient
C_m	Pitching moment coefficient
C_n	Yawing moment coefficient
D	Propeller diameter, Drag force (aircraft)
F	Prandtl's tip loss factor
F_X	Axial force
F_Y	Transverse force
F_Z	Normal force
F_d	Fixture drag force

J	Advance ratio
L	Lift force
L_{cg}	Rolling moment about cg location
M_X	Axial moment
M_{cg}	Pitching moment about cg location
M_Y	Transverse moment
M_Z	Normal moment
N_{cg}	Yawing moment about cg location
P	Propeller Power
P_i	Propeller induced power
P_o	Propeller thrust power
Q	Propeller torque
S_w	Aircraft's wing area
T	Propeller thrust
V	Forward velocity
V_E	Effective velocity = $\sqrt{V_R^2 + w^2}$
V_R	Resultant velocity = $\sqrt{(\omega r)^2 + V^2}$
V_T	Blade tip velocity
Y	Side force
b	Sectional blade chord length
b_w	Aircraft's wing span
c_w	Aircraft's wing chord length
dD	Differential drag force
dF_Q	Differential torque force
dL	Differential lift force
dT	Differential thrust
dp	Air pressure increment behind actuator disc
dr	Radial increment length of propeller blade
$f(\alpha)$	Function describes mathematical model of lift curve
h	Sectional blade thickness
$\dot{m}$	Mass flow rate
p	Air pressure far from actuator disc

p'	Air pressure at the actuator disc
$\hat{p}$	Propeller pitch
r	Sectional blade radius
w	Induced velocity at actuator disc or propeller blade
w'	Induced velocity far behind actuator disc
w_a	Axial component of induced velocity
w_t	Tangential component of induced velocity
x	Normalized sectional blade radius
x_T	Normalized propeller tip radius
x_{cg}	Distance between *cg* location and measurement point projected along x-body axis
x_h	Normalized propeller hub radius
z_{cg}	Distance between *cg* location and measurement point projected along z-body axis
$\Delta\alpha$	Angle of attack correction
$\Delta \mathrm{c}_L$	Lift coefficient correction
$\Delta\theta$	Correction factor due to tangential induced velocity
Γ	Bound vortex circulation
α	Angle of attack
α_i	Induced angle of attack
β	Sectional blade angle
η	Efficiency
η_i	Ideal efficiency (Momentum theory)
κ	Goldstein's circulation factor
λ	Local advance ratio
ϕ	Flow angle
ρ	Air density
σ	Sectional blade solidity
$\sigma_{[\bullet]}$	Standard deviation

Appendix B

Wind Tunnel Measurement Errors

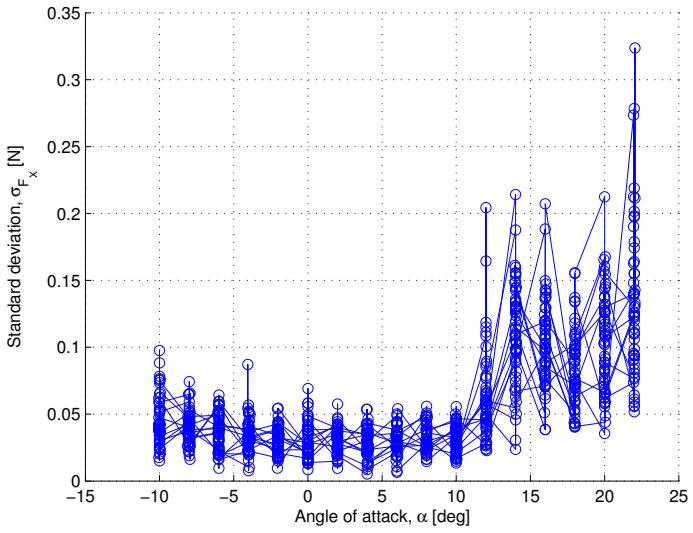

Figure B.1: Wind tunnel axial force measurement errors.

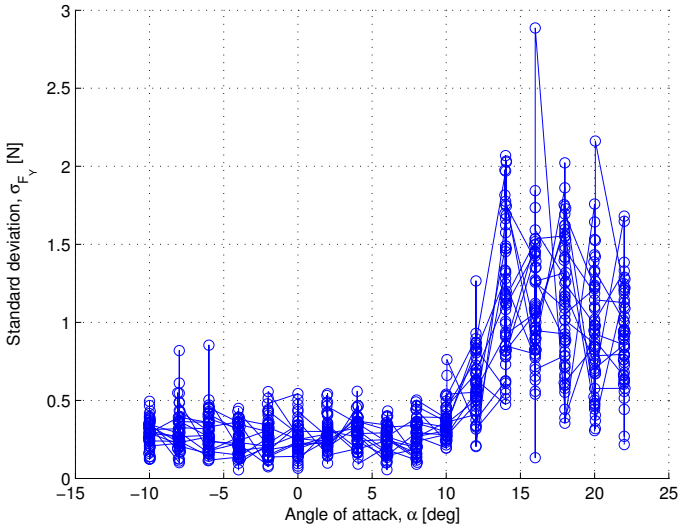

Figure B.2: Wind tunnel transverse force measurement errors.

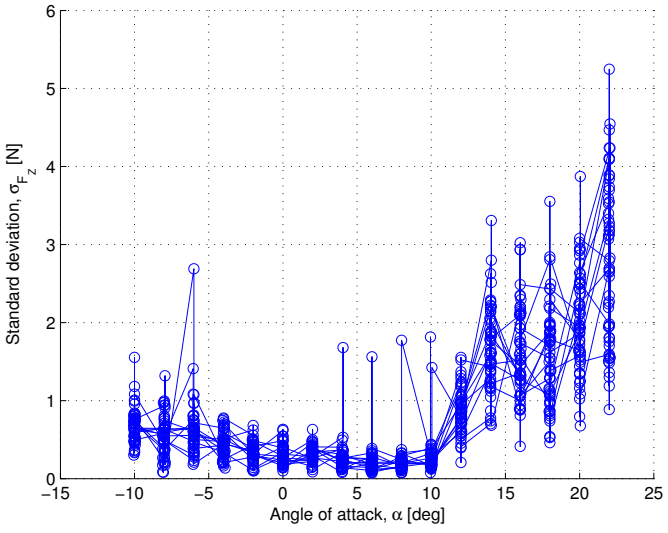

Figure B.3: Wind tunnel normal force measurement errors.

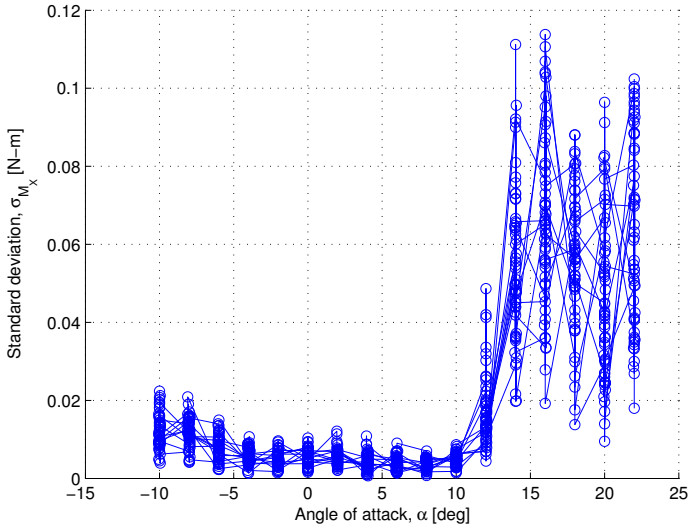

Figure B.4: Wind tunnel axial moment measurement errors.

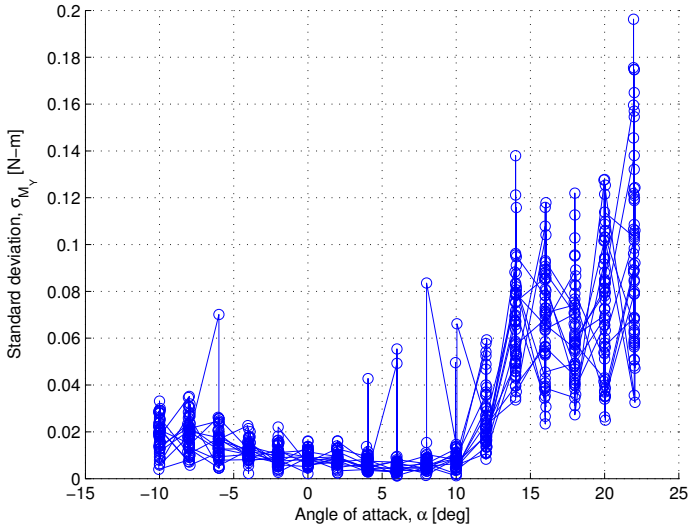

Figure B.5: Wind tunnel transverse moment measurement errors.

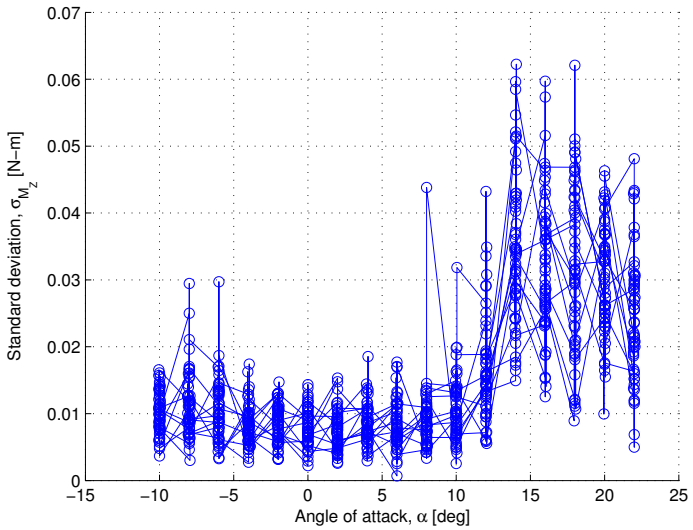

Figure B.6: Wind tunnel normal moment measurement errors.